The Thesis Committee for David Riegler
certifies that this is the approved version of the following thesis:

High frequency microrheology with optical tweezers

APPROVED BY

SUPERVISING COMMITTEE:

Mark G. Raizen, Supervisor

Manfred Fink

High frequency microrheology with optical tweezers

by

David Riegler, B.S.

THESIS

Presented to the Faculty of the Graduate School of
The University of Texas at Austin
in Partial Fulfillment
of the Requirements
for the Degree of

MASTER OF ARTS

THE UNIVERSITY OF TEXAS AT AUSTIN
August 2015

Dedicated to my family.

Acknowledgments

First of all, I would like to thank my supervisor Dr. Mark Raizen who gave me the opportunity to work in his amazing group. His passion about physics is contagious and created a very motivating atmosphere in the lab. I learned incredibly much with this project and had a really good time.

During my stay in Austin, I closely worked along with Jianyong Mo, who has been a great mentor and friend. His insight and experience in physics is outstanding and I am very grateful for sharing so much knowledge and ideas with me and the effective teamwork.

I greatly appreciate the prior work of Simon Kheifets and Akarsh Simha for leaving me a well-functioning experimental setup. I worked along with Simon for about a month and he as been a fantastic teacher, making me familiar with the setup. Akarsh has been around for most of the year and always had an open ear for questions about the control software and flowcells. I want to especially thank you for all the good conversations and discussions about hydrodynamic theory which were so enriching and pleasurable.

Special thanks to Georgios Stratis and Igal Bucay who worked on an experiment right next to me for always patiently wearing laser safety goggles when I needed the lasers on and all the fun conversations while working in the lab. Moreover I appreciate the help of the rest of the Raizen group:

Kevin Melin, Karl Burkhardt, Rodrigo Castillo-Garza, Jamie Gardner, Erik Anciaux, Yu Lu, Alina Blinova, David Dunsky, Tharon Morrison and especially Jimmy Kennington, who participated in the microrheology project. You all contributed to the positive atmosphere which made my stay so enjoyable.

I want to thank all members of the CNLD, especially Olga Vera and the graduate coordinator Matthew Ervin for their administrative help, reminding me of important deadlines and solving any occurring problem with great patience. Further I want to thank Dr. Manfred Fink who originally initiated this exchange program which gives three students from the Julius-Maximilians-Universitaet Wuerzburg the opportunity to come to this amazing university every year. I also acknowledge Dr. Giorgio Sangiovanni who is currently the counterpart for the exchange program in Wuerzburg. I also want to thank Ursula Shahmary from the international office in Wuerzburg who was a great help in doing all the paperwork for studying abroad and the German Academic Exchange Service (DAAD) for the financial support.

Moreover I would like to thank my roommates and friends in Austin who made it fun to explore the American culture and my girlfriend and all my friends in Germany who never let me down despite the far distance.

Finally I want to thank my family for their endless love and support in everything I do.

David Riegler

The University of Texas at Austin, August 2015

High frequency microrheology with optical tweezers

David Riegler, M.A.
The University of Texas at Austin, 2015

Supervisor: Mark G. Raizen

This thesis presents a method to measure the linear viscoelastic response of fluids by tracking and analyzing the thermal, Brownian motion of suspended tracer particles, known as passive microrheology. The particle is confined in a harmonic optical trap and its one dimensional trajectory is obtained by a home-built split beam detection system, which works similar but responds faster than position detection with commercial quadrant photodiodes. The theory which is necessary to convert the particle trajectory into the complex shear modulus is derived in detail, pointing out that the commonly used Mason-Weitz method needs to be modified in order to obtain correct results at high frequencies due to hydrodynamic effects of the fluid. It follows a detailed explanation of the data analysis procedure which is verified for water up to angular frequencies of $10^7\, rad/s$ in very good agreement with the theory. Finally, there is an outlook how to apply the method to actual complex fluids.

Table of Contents

List of Figures

Chapter 1

Introduction

Rheology, as an interdisciplinary subject, is the study of the flow of matter and its response to external forces, especially in the liquid phase. Simple Newtonian fluids, such as water, can be well approximated as purely viscous and simple solids can be described with Hooke's law as purely elastic. However, many materials such as polymer solutions, gels and various bio materials, referred as non Newtonian, complex or viscoelastic fluids contain both, viscous and elastic elements. The linear response of the fluid can be described by means of the complex shear modulus $G^*(\omega)$ which is the ratio of stress $\sigma(\omega)$ and strain $\gamma(\omega)$, no matter which has been imposed and which has been measured [1]

$$\sigma(\omega) = G^*(\omega)\gamma(\omega). \tag{1.1}$$

The real part of the complex shear modulus corresponds to the elasticity of the fluid whereas the imaginary part contains information about its viscous behavior. Its determination is the main goal of microrheology.

In traditional bulk rheometry, one usually applies a controlled stress or strain to measure the response of the fluid [2]. Passive microrheology, on the other side, is based on observing the thermally driven Brownian motion of a tracer particle, usually a micron sized sphere, in a fluid and inferring viscoelastic properties from the particle's trajectory. There are numerous advantages of microrheology compared to traditional rheology. First of all, microrheology can be performed in microscopic, complex environments, requiring very small sample volumes in the order of microliters, where conventional rheometry provides only a macroscopic average [3]. Also it is less invasive which makes it attractive to biological applications. Moreover, microrheology is capable of accessing a much broader range of frequencies. A downside is, that it requires certain optical properties, such as at least partial light transparency of the fluid and low laser absorption of the tracer particle [4]. Microrheology has found applications in e.g. studying the viscoelasticity of living cells [5, 6] or biopolymers in pharmaceutical applications [7]. Viscoelastic moduli at high frequencies are also of interest in industrial applications, for example ink-jet printing [8].

In order to perform microrheology, one has to determine the mean square displacement $\langle \Delta x^2(t) \rangle = \langle [x(t) - x(0)]^2 \rangle$ of the tracer particle. Over the years many techniques to measure a particles trajectory have been developed, for example video-particle tracking, diffusing wave spectroscopy or confining the particle in an optical trap and obtaining its displacement with a quadrant photo diode [9]. Here, an optical tweezer setup has been applied, but instead of a commonly used quadrant photo diode, the particle position is measured with a home-built split beam detection system, which responds faster than commercially available quadrant photodiodes. The experimental setup and data acquisition procedure is explained in Chapter 2.

The most common way to obtain the complex shear modulus form observation of Brownian motion was proposed by Mason and Weitz in 1995, relating it to the Laplace transform of the mean square displacement with a generalized Stokes-Einstein relation [10]. However, their formula is not accurate at high frequencies, where hydrodynamic effects such as an effective mass of the bead and hydrodynamic memory of the fluid become important, as it was already pointed out by Felderhof in 2009 [11, 12] and more recently by Indei et al. [13]. Chapter 3 presents a detailed derivation of the theory of Brownian motion in complex fluids, leading to the exact equation to compute the complex shear modulus with the Laplace transform of the mean square displacement.

Chapter 4 deals with the data analysis procedure, including an optimization of the numerical algorithm and dealing with noise. The method is verified with water, yielding correct results up to an angular frequency of $10^7\,rad/s$ and with acetone up to $\omega = 5 \times 10^6\,rad/s$. Finally, it is outlined how to apply the method to actual complex fluids.

Chapter 2

Experimental setup

This chapter explains the experimental setup, which is capable of recording position trajectories of Brownian particles at very short times, which is necessary to reach high frequencies in microrheology. The main idea is to hold a microsphere in an optical trap in order to record a one dimensional trajectory over a long time to obtain a good statistical time average. The displacement of the particle is measured with a home-built split beam detection system in which the trapping beam also serves as the detection beam. The first section summarizes the physical principle of optical tweezers. The following section explains the method of split beam detection and the data acquisition process. The last section contains technical details about the setup.

2.1 Physical principle of optical tweezers

The physical principle of optical tweezers is based on radiation pressure which was first deduced by James Clerk Maxwell from the electromagnetic theory in 1873 [14] and experimentally verified in 1901 [15, 16]. The resulting force on a particle caused by a light source with a power of 1 W can be estimated by the force on a full reflecting mirror which is approximately 7 nN

[17]. This is very weak in absolute terms, the development of lasers in the 20th century, however, makes it possible to focus high power radiation on micron sized particles and due to their small masses, the radiation force can be five orders of magnitude higher than the gravitational force. Ashkin was the first person to observe the acceleration and trapping of transparent micron sized particles with focused laser beams in 1970 [18]. In 1986, Ashkin et al. reported the first successful, stable trapping of dielectric particles by a single, focused laser beam with the gradient force [19]. This technique was further developed over the years, for example to manipulate viruses and bacteria [20] and has become a standard tool in biophysics known as the optical tweezer [17].

A relatively simple physical explanation for the optical trapping of a sphere with diameter d can be found in the ray optics limit $d \gg \lambda$ and the Rayleigh approximation $d \ll \lambda$ where the particle is treated as a point dipole [19]. In most experiments, nevertheless, the diameter is comparable to the laser wavelength λ and one has to apply the electromagnetic theory which is very complex. T. Nieminen et al. have developed a computational toolbox to obtain numerical results with generalized Lorentz-Mie theory in that regime [21] which will, however, not be further discussed in this thesis.

2.1.1 Ray optics approximation

When the bead diameter is much larger than the laser wavelength, the trapping can be explained by ray optics [19, 22]. As a ray of photons is refracted, it leaves the dielectric sphere in a different angle than it entered and

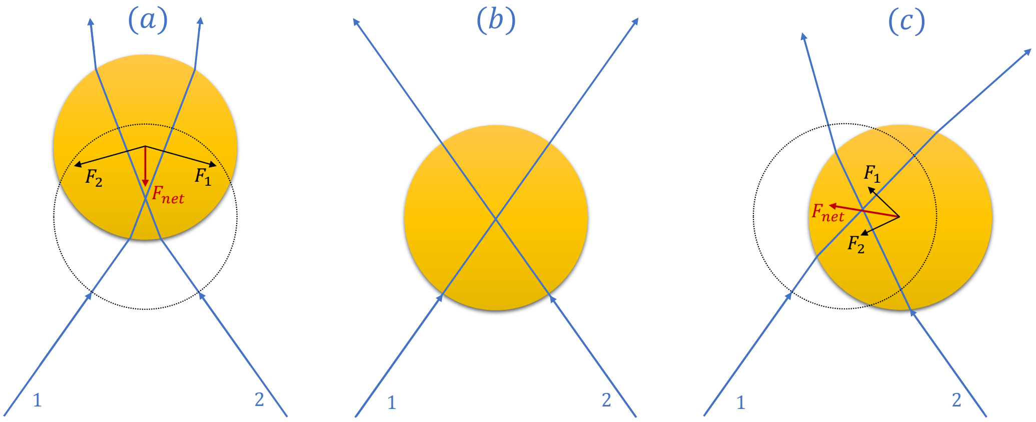

Figure 2.1: Neglecting reflection, this figure illustrates, that any displacement of the dielectric sphere from the laser focus leads to a net force back to the trap center due to momentum transfer of photons to the bead by regarding two typical rays. If the bead is in the focus, there is no resulting force on it and the rays are perpendicular to the surface (b). If the bead is displaced axially in direction of the laser beam, the beam converges compared to the equilibrium and the resulting recoil points in opposite direction of the beam propagation (a). For displacement of the bead axially in the other direction, the rays spread out behind the bead and the net force points again to the center of the trap. If the bead is displaced laterally, the net force also leads back to the equilibrium position (c).

thus has changed its momentum which is transferred to the bead as recoil. The total momentum change is obtained by summing over all rays. Figure 2.1 illustrates, neglecting reflection from the sphere, that any displacement of the bead out of the laser focus results in a net force which drags it back into the focus. Consequently a single, focused laser beam can create a stable 3D trap. Since the total number of photons refracted is proportional to the laser intensity, the trapping strength is proportional to the laser power. In reality, there is also reflection from the bead surface which leads to an additional force in direction of the beam propagation. If this force is stronger than the restoring force due to refraction (Figure 2.1 (a)), the trap potential has no minimum, the bead is pushed backwards and a stable trap doesn't exist.

2.1.2 Rayleigh approximation

A quantitative, analytical description with Rayleigh scattering theory can be done in the limit $d \ll \lambda$ where the trapped particle is treated as a point dipole [19, 23]. The following sums up the results given in [23] yielding two different forces on the particle and comments on the stability of the trap.

The intensity of a Gaussian laser beam with fundamental mode TEM_{00} and linear polarization of the electric field in x-direction, propagating in z-direction, with focus spot at $z = 0$ in paraxial approximation is given by [23]

$$\mathbf{I}(r,z) = \frac{2P}{\pi w^2(z)} \exp\left(-\frac{2r^2}{w^2(z)}\right) \hat{\mathbf{z}}. \tag{2.1}$$

$w(z)$ is the radius where the intensity drops to $1/e^2$ of its centered value

$$w(z) = w_0 \sqrt{1 + \left(\frac{z\lambda_0}{\pi w_0^2 n_f}\right)^2} \tag{2.2}$$

with vacuum laser wavelength λ_0, index of refraction n_f of the surrounding fluid and beam waist radius w_0 at the focus $z = 0$. Because of the oscillating electric field, the induced point dipole radiates and scatters light and the consequent change of the energy flux resulting in momentum transfer leads to the scattering force [23]

$$\mathbf{F}_{scat}(r,z) = \frac{128\pi^5}{3} \frac{n_f^5}{c\lambda_0^4} \alpha^2 \mathbf{I}(r,z). \tag{2.3}$$

α is the polarizability of a dielectric sphere with radius R and ratio $m = n_p/n_f$ between the index of refraction of the particle and the fluid

$$\alpha = R^3 \frac{m^2 - 1}{m^2 + 2}. \tag{2.4}$$

The gradient force is due to the Lorentz force on the induced dipole [23]

$$\mathbf{F}_{grad}(r, z) = \frac{2\pi n_f}{c} \alpha \nabla |\mathbf{I}(r, z)|. \tag{2.5}$$

Similar to the effect of refraction in the ray optics picture, it forms a trapping potential, pushing the bead to the focus where the laser intensity has its maximum. The scattering force, however, corresponding to the reflection in the ray optics picture, acts in direction of the laser propagation and pushes the bead out of the trap. With $\mathbf{F}_{net} = \mathbf{F}_{grad} + \mathbf{F}_{scat}$, it requires $|F_{z,grad}| > |F_{z,scat}|$ in order to form a stable trap. Since $\mathbf{F}_{grad} \propto R^3$ and $\mathbf{F}_{scat} \propto R^6$ it is easier too fulfill this condition for smaller beads. However, since the trapping potential decreases for smaller radii, but the thermal energy is independent of the radius by the Equipartition theorem, beads which are too small cannot be trapped stably either. Comparing the two forces with regard to the index of refraction ratio yields, that the scattering force increases faster then the gradient force for higher m. The ratio between gradient force and scattering force can be increased by reducing the beam waist w_0, which requires a high numerical aperture.

A stable trap can be approximated harmonically for $|\mathbf{x}| \ll w_0$ by expanding the intensity to the second order around the equilibrium position

$\mathbf{x} = 0$. The resulting trap constants, neglecting the scattering force, are

$$k_{x,y} = \frac{8 n_f \alpha P}{c w_0^4} \tag{2.6}$$

$$k_z = \frac{4 \lambda_0^2 \alpha P}{\pi^2 c n_f^2 w_0^6}. \tag{2.7}$$

2.2 Split beam detection

Observing Brownian motion at short timescales requires a detector with very high spacial and temporal resolution. For trapped Brownian motion, position detection with a quadrant photodiode has become a standard tool, achieving subnanometer resolution [24–27].

The laser is focused in order to create an optical trap and then recollimated by a second objective with focal point at the trap focus and the intensity profile is detected in the back focal plane. When the particle is displaced in the plane normal to the optical axis with respect to the trapping center, it changes the angular intensity distribution of the outgoing beam. In a quadrant photodiode, the photosensitive area is split into four quadrants ($\pm x$ and $\pm y$ relative to the optical axis) of which each photo current can be amplified separately. For small displacements of the bead, the horizontal deflection is proportional to the total power difference of the left and right halves and the vertical displacement is proportional to the difference of the top and bottom halves. A theoretical one dimensional description of the detection method was given by Gittes and Schmidt, describing the intensity changes by interference effects of scattered and transmitted light in the Rayleigh regime

[24]. Under certain approximations, the result is [25]

$$\frac{I_+ - I_-}{I_+ + I_-} \approx 32\sqrt{\pi}\frac{n_f \alpha}{\lambda_0 w_0^2}\frac{x}{w_0}e^{-(x/w_0)^2}. \tag{2.8}$$

which is linear for $x \ll w_0$, where $I_{+,-}$ is the integrated intensity on the +x (-x) side. The displacement of the bead from the trapping center in Brownian motion can be estimated with the root mean square by the Equipartition theorem $x_{rms} \equiv \sqrt{\langle x^2 \rangle} = \sqrt{k_B T/k}$ with k being the trapping strength, which is of the order of tens of nanometers and in the linear regime of the detector.

The main limitation in bandwidth of quadrant photodiodes to around 150 kHz is their capacitance. A single photodiode can achieve a higher bandwidth, because the beam can be focused to a much smaller photosensitive area leading to a lower capacitance of the diode and a faster response. This was exploited to develop a faster detection system in the Raizen group. The main idea is to physically split the laser beam and focus both halves of the beam on a fast, balanced photodetector which amplifies the intensity difference of the inputs. The first generation of the detection system used a fiber bundle to split the beam [28]. More effectively, as in the current setup, the beam is split by a mirror with a sharp edge (D-shaped mirror) which is easier and causes less noise [29]. This setup only allows one dimensional detection, but could simply be extended to two dimensions by adding another D-shaped mirror. However, this is not necessary for the purpose of this thesis, since the equations of motion in the theory of Brownian motion have no coupling between the Cartesian coordinates which makes a one dimensional trajectory sufficient.

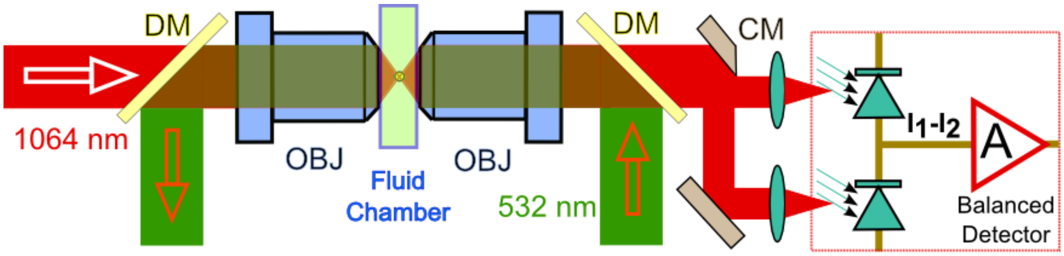

Figure 2.2: Schematic of the split beam detection system. A 1064 nm infrared laser beam is focused and re-collimated by two identical objectives, forming an optical trap. In between is a fluid chamber in which the trapped Brownian motion takes place. The detection beam is then split into two equal halves by a D-shaped mirror (CM) and detected by a fast balanced detector, amplifying the intensity difference of the input beams. A second, counter propagating laser beam can be introduced with two dichroic mirrors (DM) to cancel the scattering force if it is necessary in order to form a stable trap. Graphic from Jianyong Mo [30].

In order to obtain a clean signal, the D-shaped mirror has to be aligned carefully. If it doesn't split the beam in two equal halves, it effectively adds a constant displacement of the bead and also increases laser intensity noise. The limiting noise at high frequencies is photon shot noise which is due to the quantization of light. The arrival rate of photons is a Poisson process with variance $\langle \Delta N^2 \rangle = N$ [31]. Consequently the signal to noise ratio is [29]

$$SNR \propto \sqrt{N} \propto \sqrt{P}. \tag{2.9}$$

At short timescales, one simply “runs out of photons”. Consequently, the noise level can be reduced by increasing the detection power.

The detection setup contains two different balanced photodetectors. A DC-coupled commercial detector (Thorlabs model:PDB110C) with a damage

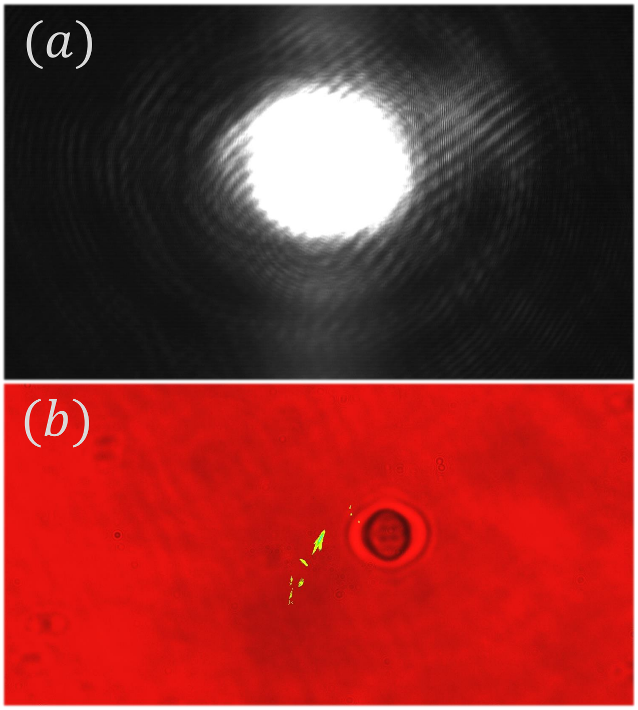

Figure 2.3: (a): CCD image of the beam profile before splitting at the the D-shaped mirror. (b) CCD image of a trapped silica bead in water with $R \approx 1.5\,\mu m$.

threshold of 5 mW per photodiode and a home built AC-coupled balanced detector. The AC-detector has been optimized for high frequencies, allowing a power of up to 100 mW per photodiode, which is much more than most commercially available detectors [29], to reduce shot noise. In order to keep the peak to peak voltage within the limits of the op-amp and the digitizer at such high input power, a high pass filter has been added to the electronics of the detector to suppress low frequency noise. Since the signal is strongly modified at low frequencies by the filter, it has to be deconvoluted by dividing

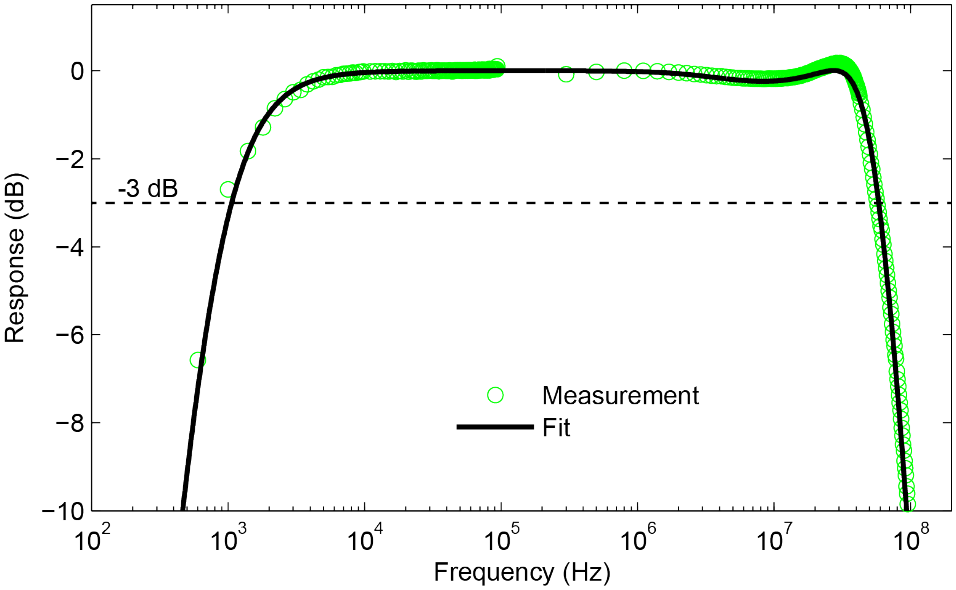

Figure 2.4: Transfer function of the AC-detector and its fit. Graphic from Simon Kheifets [29].

the power spectral density (PSD) of the signal by the response function of the detector. To do so, the transfer function has been measured and fitted [29].

The output of both detectors is digitized using an ultra low noise ADC board (GaGe model: Razor 1622 Express CompuScope) with a maximum sampling rate of 200 MSa/s and 128 million consecutive samples. The data acquisition is controlled by a LabVIEW program which has mostly been written by Akarsh Simha. The resulting data is an array of voltages, equally spaced in time, which are proportional to the displacement of the bead. The AC detector cannot give low frequency information because of the high pass filter, but by combination of both detectors, the whole frequency range can be accessed.

2.3 Technical details

This section provides technical details about the lasers, trapping optics and the control of the experiment. It also gives a tutorial how to build flow cells in which the Brownian motion takes place. A more detailed description can be found in the dissertation of Simon Kheifets [29] who mainly designed the experimental setup.

2.3.1 Lasers and optics

The laser used for trapping and detection is a 1064 nm YAG (Innolight, model: Mephisto) with a maximum power of 1.2 W and the beam is fiber coupled into a polarization maintaining single mode fiber (Thorlabs, P3-1064 PM-FC-5) in order to reduce pointing noise. The laser power can be set to the desired level with a waveplate and a polarization beam-splitter, controlled by the LabVIEW program. The maximum achievable trapping power is about 300 mW and the maximum detection power about 150 mW due to absorption in the objectives. The setup includes a second, fiber coupled, counter propagating laser (Coherent, model: Verdi V-10, 512 nm) which can be used if trapping is not possible with a single beam because of the scattering force. Its power is controlled with an acousto optic modulator. The $1/e^2$ waist of both collimated beams after the fibers is about 1.5 mm. The beams are focused and recollimated using two identical finite-conjugate water-immersion microscope objective lenses (LOMO, model: OM-25). The nominal numerical aperture is 1.23 with a focal length of 2.5 mm and a working distance of distance $140\,\mu m$.

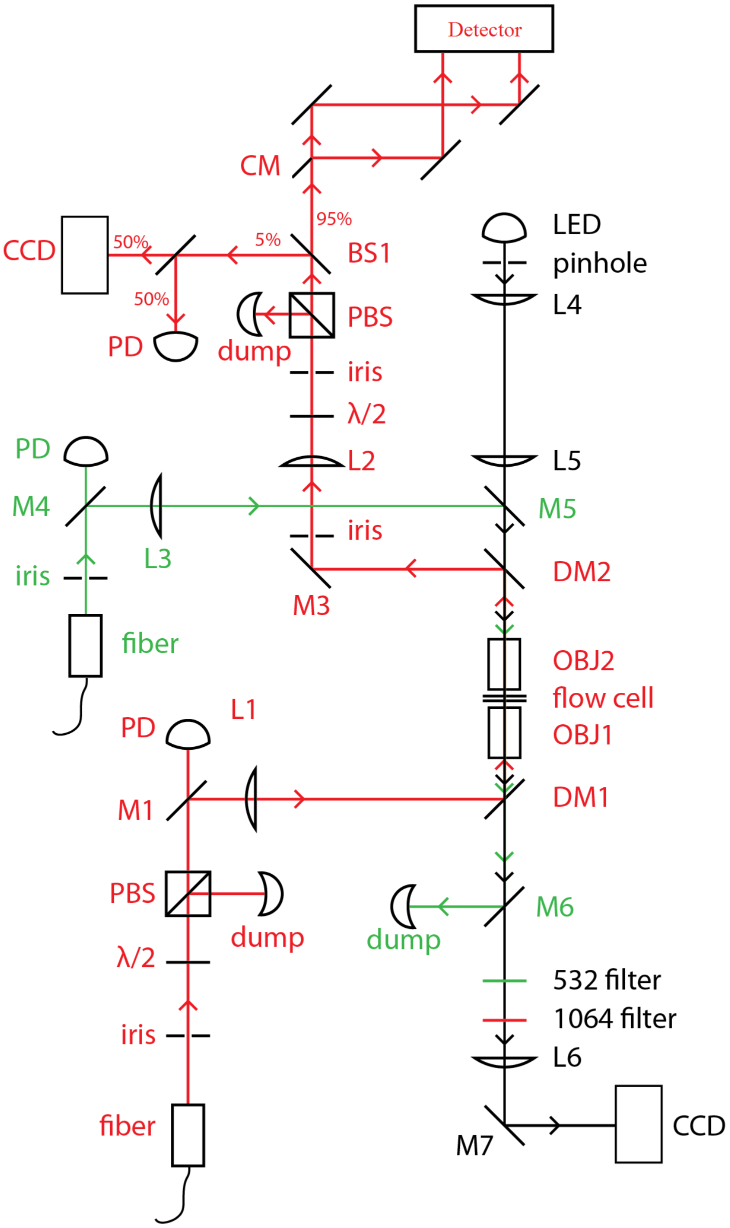

Figure 2.5: Detailed schematic of the experimental setup. The red line is the optical path of the 1064 nm laser, the green line is the optical path of the 532 nm laser. PBS: polarization beam splitter, PD: photodiode, L: lens, OBJ: objective, DM: dichroic mirror, CCD: CCD camera, CM: D-shaped mirror. Graphic from Simon Kheifets [29].

A CCD camera provides images of the trap region with an 100 mW red LED as light source. The imaging helps to find and trap beads, provides information about the bead size, possible contaminants and is useful for the laser alignment process.

The D-shaped mirror used to split the beam is from Thorlabs, model BBD05-E03. The power to the detector is controlled with a waveplate and polarization beam splitter. The beam profile at the D-shaped mirror is monitored with a CCD camera.

2.3.2 Flow cells

Since the working distance of the objectives is only $140\,\mu m$, the flow cell in which the Brownian motion takes place must be extremely narrow ($\sim 280\,\mu m$). To achieve that, it is constructed with a layer of Nescofilm (Bando Chemical Ind. LTD., thickness $\sim\ 80 \mu m$) and two No. 0 microscope coverslips (Gold Seal model: 24X60-0-002, $24\,mm \times 60\,mm$, thickness: $\sim 100\,\mu m$). To create an outflow and inflow, holes ($d \sim 1\,mm$) are drilled in a stack of coverslips with a diamond drill with very high speed.

The desired shape of the chamber is cut into the Nescofilm with a scalpel. Then, it is sandwiched between a drilled an undrilled coverslip and put on a lab hot plate under pressure at $130°C$ for around 6 minutes. This way the Nescofilm melts and creates a sealed volume. The flowcell is then mounted on an aluminium bracket with holes aligned to the in- and outflow of the cell. To connect it, silicone tubing is inserted into drilled nylon setscrews

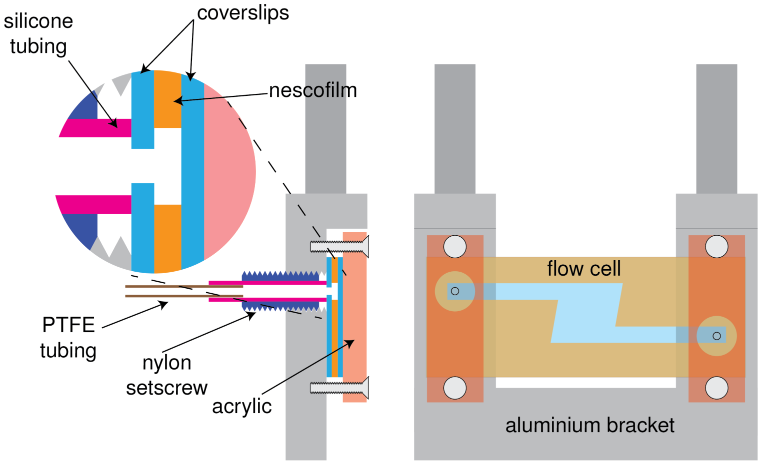

Figure 2.6: Illustration of a flow cell mounted on the aluminium bracket. Graphic by Simon Kheifets [29].

and screwed into the aluminium bracket, sealing the holes of the coverslip by pressure. The silicone tubing is connected to PTFE tubing and finally to a syringe to fill the chamber with the desired microsphere suspension with a pump. The aluminium bracket is placed on a 3-axis translation stage, so that the chamber position can be changed without affecting the optics.

As it turns out, a clean flowcell is essential to minimize low frequency noise which is mostly caused by mechanical vibration of the optics resulting in relative motion of the laser beam to the D-shaped mirror, leading to noise peaks of the PSD at the resonance frequencies. This effect is especially magnified, if dirt in the chamber is trapped additionally to be bead, or if there is contamination on the chamber walls which modifies the laser beam profile. Low frequency noise can be transferred through the ground or air flow e.g. through air conditioning. There is no easy way to eliminate it but to further minimize it, the whole setup is built on an air-floated optical table with maximum damping (TMC, Steel honeycomb core, model number: 78-676-02). To make flowcells as clean as possible, coverslips are cleaned in an ultrasonic cleaner with isopropanol and acetone to remove dust and remains from the drilling. It is also important to fix the tubing with tape on the way to the pump because it is otherwise also sensitive to vibration and can affect the Brownian motion in the chamber. Figure 2.7 compares the PSD and trajectory of a Brownian particle for a noisy and a clean measurement.

In order to avoid boundary effects the bead has to be trapped in the center of the flowcell. This way the distance to the nearest boundary is about $40\,\mu m$ which is much larger than the radius of the bead, so that boundary effects are negligible.

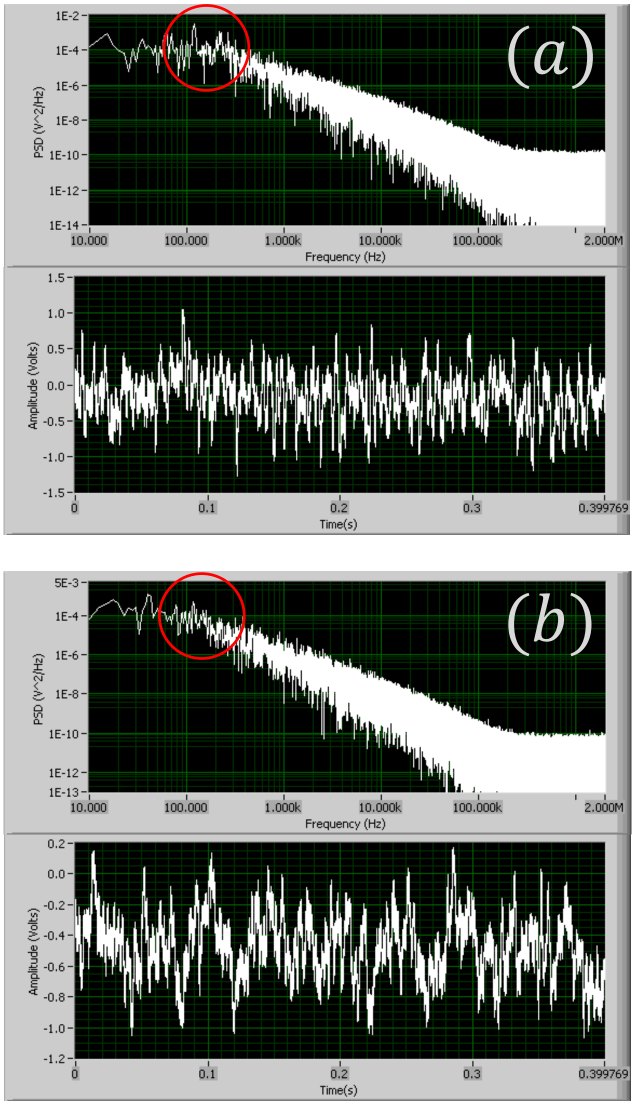

Figure 2.7: This figure shows the PSD and the position trajectory (in volts) of a trapped Brownian particle, as it is produced in real time by the LabVIEW program. (a) is the result of a dirty and (b) the result of a clean chamber. As one can see in the red circled area, both measurement have a noise peak at 120 Hz, but it is much stronger in measurement (a). The position trajectory in (a) looks very periodic due to the high peak, while it appears much more random in (b) as it should for Brownian motion.

Chapter 3

Theories on Brownian motion

Brownian motion is the random movement of particles dispersed in a fluid which results from the collisions with surrounding atoms or molecules. It is named after Robert Brown who initially observed the transport phenomenon with pollen in water under a microscope in 1827 [32]. To understand how a complex fluid affects the motion of a tracer particle in order to perform microrheology, one first has to study Brownian motion in Newtonian fluids. The first section of this chapter presents principles of statistical mechanics of stationary processes which are true in general but required to understand Brownian motion. Afterwards the first theory which was suggested by Einstein is summarized and the more extensive Ornstein-Uhlenbeck theory on Brownian motion based on a Langevin equation is explained. To make this theory applicable for liquids, hydrodynamic effects have to be taken into account, which is done in section three. Subsequently, the hydrodynamic theory is further modified to include complex fluids. Predictions of the theory are illustrated with a simple model of a complex fluid. Finally, section five derives the equations to obtain linear viscoelastic moduli from the observation of Brownian motion.

3.1 Statistical mechanics of correlation functions

In this section, it will be illustrated how the most important quantities to characterize Brownian motion which are correlation functions and power spectral densities are related. Moreover, the reader will learn about the fluctuation-dissipation theorem, which was published by Kubo in 1966.

3.1.1 Correlation functions of stationary processes

Since Brownian motion involves collisions with trillions of surrounding molecules, the trajectory of a single particle is chaotic and cannot be predicted. Consequently, theories aim on statistical quantities which are in the following denoted with brackets $\langle ... \rangle$. These formally represent the ensemble average which is the average over many independent systems with the same initial conditions or equivalently a statistical average over a certain probability distribution. Since Brownian motion is a stationary process and we assume it to be ergodic, however, the ensemble average can be replaced by the time average [33]

$$\langle \xi \rangle = \int p(\xi) \xi d\xi = \lim_{T \to \infty} \frac{1}{T} \int_{-T/2}^{T/2} \xi(t) dt \tag{3.1}$$

for any stochastic process ξ where $p(\xi)$ is the belonging probability density and T is the recording time. Accordingly, the correlation function of a random variable is defined by

$$C_\xi(t) \equiv \langle \xi(t) \xi(0) \rangle = \lim_{T \to \infty} \frac{1}{T} \int_{-T/2}^{T/2} \xi(t+\tau) \xi(\tau) d\tau. \tag{3.2}$$

For stationary processes, correlation functions are symmetric in time

$$\langle\xi(t)\xi(0)\rangle = \langle\xi(t+\tau)\xi(\tau)\rangle \underbrace{\iff}_{\tau=-t} \langle\xi(t)\xi(0)\rangle = \langle\xi(-t)\xi(0)\rangle. \tag{3.3}$$

Note, that the random variable ξ in Brownian motion it typically the position x or the velocity v of the particle.

3.1.2 The Wiener-Khinchin theorem

Besides correlation functions, power spectral densities are of great importance in characterizing Brownian motion. The power spectral density (PSD) of a variable ξ is defined as the absolute square of its Fourier transform [34]

$$S_\xi(\omega) \equiv |\mathcal{F}_t\left\{\xi(t)\right\}|^2 = \lim_{T\to\infty}\frac{1}{T}\left|\int_{-T/2}^{T/2} e^{i\omega t}\xi(t)dt\right|^2. \tag{3.4}$$

Descriptive, the PSD illustrates how much intensity of the signal $\xi(t)$ can be decomposed by an infinitesimal frequency window around ω. The Wiener-Khinchin theorem relates the correlation function to the according PSD with Fourier transformation [33, 35, 36]

$$S_\xi(\omega) = \int_{-\infty}^{\infty} e^{i\omega t}\langle\xi(t)\xi(0)\rangle dt. \tag{3.5}$$

A proof can be found in Appendix A.1. With the time symmetry of correlation functions follows

$$S_\xi(\omega) = S_\xi(-\omega) = 2\int_0^\infty \cos(\omega t)\,\langle\xi(t)\xi(0)\rangle dt \tag{3.6}$$

and with inverse Fourier transform

$$\langle\xi(t)\xi(0)\rangle = \frac{1}{2\pi}\int_{-\infty}^{\infty} e^{-i\omega t}S_\xi(\omega)d\omega = \frac{1}{\pi}\int_0^\infty \cos(\omega t)\,S_\xi(\omega)d\omega. \tag{3.7}$$

Further one finds [33]

$$S_{\dot{\xi}} = \omega^2 S_\xi(\omega) \Rightarrow S_v = \omega^2 S_x(\omega) \tag{3.8}$$

which can be directly shown with Eq. (3.7):

$$\langle \xi(t)\xi(t')\rangle = \langle \xi(t-t')\xi(0)\rangle = \frac{1}{2\pi}\int_{-\infty}^{\infty} e^{-i\omega(t-t')} S_\xi(\omega) d\omega,$$

applying $\frac{\partial}{\partial t}\frac{\partial}{\partial t'}\Big|_{t'=0}$ on both sids leads to

$$\langle \dot{\xi}(t)\dot{\xi}(0)\rangle = \frac{1}{2\pi}\int_{-\infty}^{\infty} \omega^2 e^{-i\omega t} S_\xi(\omega) d\omega.$$

Comparing to Eq. (3.7) with $\xi \to \dot{\xi}$ yields Eq. (3.8).

3.1.3 The fluctuation-dissipation theorem

In 1966, R. Kubo published a relation between response functions and correlation functions with linear response theory. This work plays a major role in the theory of Brownian motion, but can also be applied to many other systems. The admittance, also called mobility $\mu(\omega)$ is related to the velocity autocorrelation function by [37]

$$\mu(\omega) = \frac{1}{k_B T}\int_0^{\infty} e^{i\omega t}\langle v(t)v(0)\rangle dt \tag{3.9}$$

which is often called the first fluctuation-dissipation theorem. The admittance $\mu(\omega)$ is the response function of the velocity to an external force [33]

$$\langle \tilde{v}(\omega)\rangle \equiv \mu(\omega)\tilde{F}_{ext}(\omega). \tag{3.10}$$

Kubo's theory also provides a relation between the friction kernel $\gamma[\omega]$ and the random, thermal force $F_{th}(t)$ which will be introduced in the next section [37]

$$\gamma[\omega] = \frac{1}{k_B T} \int_0^{\infty} e^{i\omega t} \langle F_{th}(t) F_{th}(0) \rangle dt \tag{3.11}$$

Additionally applying Eq. (3.6) yields

$$S_{Fth}(\omega) = 2 k_B T \mathrm{Re} \left\{ \gamma[\omega] \right\}. \tag{3.12}$$

3.2 Brownian motion without hydrodynamic effects

This section contains theories on Brownian motion without hydrodynamic effects and will be generalized subsequently, following the historical development. Since the equations of motion have no coupling between the coordinates, it is sufficient to regard Brownian motion as a one dimensional problem which is true for all three Cartesian coordinates. Consequently, throughout the whole thesis $x(t)$ denotes without loss of generality the one dimensional trajectory of a Brownian particle.

3.2.1 Einstein's theory

The first theory on Brownian motion was proposed by Albert Einstein with the Diffusion equation in 1905 [38], predicting that the mean square displacement (MSD) of a Brownian particle follows the the equation

$$\langle \Delta x^2(t) \rangle \equiv \left\langle [x(t) - x(0)]^2 \right\rangle = 2Dt. \tag{3.13}$$

It characterizes how fast the particle diffuses away from its initial position. The diffusion constant is given by

$$D = \frac{k_B T}{\gamma_s} \tag{3.14}$$

with the Boltzmann constant k_B, temperature T and Stokes drag coefficient

$$\gamma_s = 6\pi\eta R \tag{3.15}$$

which is known as Stokes-Einstein relation. In Eq. (3.15), η is the viscosity of the surrounding fluid and R is the radius of the spherical Brownian particle. With Eq. (3.13) one finds the rms velocity

$$v_{rms} \equiv \frac{\sqrt{\langle \Delta x^2(t) \rangle}}{t} = \frac{\sqrt{2D}}{\sqrt{t}} \tag{3.16}$$

which diverges as t to goes to zero. Consequently Einstein's theory breaks down at short timescales.

3.2.2 Ornstein-Uhlenbeck theory of Brownian motion

In 1908, Paul Langevin suggested an alternative approach based on Newtons second law and was able to reproduce Einstein's result [39]. On the basis of such a Langevin Equation, Ornstein and Uhlenbeck developed a theory which has the same result for long times but includes a different behavior for short times which does not diverge as $t \to 0$ [40]. Their theory is yet sufficient to describe Brownian motion under certain circumstances, e.g. if the fluid is air. For a full description in a liquid, however, the theory is missing hydrodynamic effects.

For a free, spherical Brownian particle with mass m, the Langevin equation is given by [40]

$$m\ddot{x}(t) + \gamma_s \dot{x}(t) = F_{th}(t). \tag{3.17}$$

γ_s is the Stokes drag coefficient which leads to deceleration of the Brownian particle. If the drag force was the only force exerted by the fluid, however, the particle would simply lose all its kinetic energy during a characteristic time, which contradicts experimental observations. Consequently, a second force which constantly drives the Brownian motion is required. It is the random thermal force $F_{th}(t)$ which is caused by collisions with surrounding fluid molecules. The total force on the bead exerted by the fluid in Langevin equations is the sum of the drag force and the thermal force. As it is intuitively clear, these two forces cannot be totally independent, indeed, they are related with the fluctuation-dissipation theorem Eq. (3.12). Consequently, the thermal force can be further specified. Because of the symmetry of the problem, the average value should be zero at all times. Moreover the thermal force is expected to be only correlated if $|t - t'|$ is very small [40], in this case it is delta-correlated

$$F_{th}(t) = \sqrt{2k_B T \gamma_s}\zeta(t) \tag{3.18}$$

$$\langle \zeta(t) \rangle = 0 \tag{3.19}$$

$$\langle \zeta(t)\zeta(t') \rangle = \delta(t - t'). \tag{3.20}$$

The PSD of the thermal force can be be calculated with Eq. (3.5)

$$S_{F_{th}}(\omega) = \int_{-\infty}^{\infty} e^{i\omega t} \langle F_{th}(t) F_{th}(0) \rangle dt = 2k_B T \gamma_s \tag{3.21}$$

and is often referred as white noise because it doesn't depend on ω. Note that the PSD satisfies the fluctuation-dissipation theorem. Eq. (3.17) can be rewritten in terms of the velocity

$$\dot{v}(t) = -\frac{1}{\tau_p} v(t) + \frac{F_{th}(t)}{m} \tag{3.22}$$

where

$$\tau_p = \frac{m}{\gamma_s} \tag{3.23}$$

is the so called momentum relaxation time of the particle. Integrating yields

$$v(t) = v_0 e^{-t/\tau_p} + e^{-t/\tau_p} \int_0^t e^{t'/\tau_p} \frac{F_{th}(t')}{m} dt'. \tag{3.24}$$

With Eq. (3.18) it is trivial to find the velocity autocorrelation function (VACF)

$$C_v(t) = v_0^2 e^{-t/\tau_p} = \frac{k_B T}{m} e^{-t/\tau_p} \tag{3.25}$$

where v_0 has been determined by the Equipartition theorem

$$\frac{m}{2} v_0^2 = \frac{1}{2} k_B T. \tag{3.26}$$

Alternatively, the VACF can be calculated with the PSD. Eq. (3.22) after Fourier transformation reads

$$-i\omega \tilde{v}(\omega) = -\frac{1}{\tau_p} \tilde{v}(\omega) + \frac{\tilde{F}_{th}(\omega)}{m} \tag{3.27}$$

and yields

$$S_v(\omega) = |\tilde{v}(\omega)|^2 = \frac{1}{m^2} \frac{2 k_B T \gamma_s}{\omega^2 + \tau_p^{-2}}. \tag{3.28}$$

The Wiener-Khinchin Theorem Eq. (3.7) allows to conclude to the VACF

$$C_v(t) = \frac{2k_BT\gamma_s}{2\pi m^2}\int_{-\infty}^{\infty}\frac{e^{-i\omega t}}{\omega^2+\tau_p^{-2}}d\omega = \frac{k_BT}{m}e^{-t/\tau_p} \tag{3.29}$$

where the integral can be evaluated with the Residue theorem. The fact that Eq. (3.29) reproduces the result of Eq. (3.25) shows that the thermal force defined in Eq. (3.18) is, as it should, consistent with the Equipartition theorem. The MSD can be determined by once more integrating Eq. (3.24) [40]

$$\langle\Delta x^2(t)\rangle = \frac{2k_BT\tau_p^2}{m}\left(\frac{t}{\tau_p}-1+e^{-t/\tau_p}\right). \tag{3.30}$$

With a series expansion of Eq. (3.30), one finds

$$\langle\Delta x^2(t)\rangle = \frac{k_BT}{m}t^2 \qquad t \ll \tau_p \qquad \text{ballistic} \tag{3.31}$$

$$\langle\Delta x^2(t)\rangle = 2Dt \qquad t \gg \tau_p \qquad \text{diffusive} \tag{3.32}$$

which solves the earlier discussed problem of diverging velocity as $t \to 0$. the long time behavior of Brownian motion where Einsteins theory holds is called diffusive regime. The short time behavior where the inertia of the particle becomes important is referred as ballistic regime.

The Langevin equation can be further modified by adding a harmonic trap of strength k as it is realistic, if a Brownian particle is confined by an optical tweezer as discussed in subsection 2.1.2.

$$m\ddot{x}(t)+\gamma_s\dot{x}(t)+kx(t) = F_{th}(t) \tag{3.33}$$

The MSD can be found to be [41]

$$\langle\Delta x^2(t)\rangle = \frac{2k_BT}{m\omega_0^2}\left[1-e^{-t/2\tau_p}\left(\cos(\Omega t)+\frac{\sin(\Omega t)}{2\Omega\tau_p}\right)\right] \tag{3.34}$$

where

$$\omega_0 = \sqrt{\frac{k}{m}} \tag{3.35}$$

$$\Omega^2 = \omega_0^2 - (2\tau_p)^{-2} \,. \tag{3.36}$$

Note that Eq. (3.34) contains an underdamped and overdamped case, depending on whether Ω is real or imaginary. Trapped Brownian motion in a liquid is typically overdamped.

3.3 Hydrodynamic Brownian motion

To correctly describe Brownian motion in liquids, one has to solve a more general Langevin equation which can be approximated by Ornstein and Uhlenbeck's theory under certain conditions. The main differences to the previous theory are contributions of hydrodynamic memory which means that the present movement of the bead depends on its previous trajectory, and the occurrence of an effective mass due to the inertia of the surrounding fluid.

3.3.1 The generalized Langevin equation

When constructing Langevin equations, there is only one term directly determined by hydrodynamics, which is the drag force. For the theory by Ornstein and Uhlenbeck [40, 41], it was simply given by Stokes famous drag formula $F_{drag} = -\gamma_s v$ [42] which is only true for a constant velocity v. It is derived as a special solution of the incompressible Navier-Stokes equation

$$\frac{\partial \mathbf{v}(t)}{\partial t} + \mathbf{v}(t) \cdot \nabla \mathbf{v}(t) = \frac{1}{\rho} \left(\nabla p + \eta \nabla^2 \mathbf{v}(t) \right) \tag{3.37}$$

neglecting the nonlinear term and assuming a stationary velocity field of the fluid ($\partial \mathbf{v}(t)/\partial t = 0$). Dropping $\mathbf{v}(t) \cdot \nabla \mathbf{v}(t)$ can be justified for systems with low Reynolds numbers

$$Re = \frac{\rho_f l v}{\eta} \tag{3.38}$$

where l is a characteristic length and v a characteristic velocity of the system. The density of the fluid is denoted by ρ_f and η represents its dynamic viscosity. The Reynolds number for Brownian motion in water can be estimated with the diameter of the sphere as characteristic length and determining v with the Equipartition theorem. In a typical measurement with a micron sized bead at 20°C, one finds $Re \approx 10^{-5}$ which is indeed very low and justifies the above assumption. However, it turns out that the dynamic of the velocity field cannot be neglected for Brownian motion in a liquid, so that the time derivative has to be kept in order to derive a sufficient drag force which is then true for an arbitrary motion of the bead. It is preferably derived in frequency domain. A detailed derivation can be e.g be found in [43], a more advanced approach is performed Landau in and Lifshitz [44], yielding

$$\tilde{F}_{drag}(\omega) = -6\pi\eta R\tilde{v}(\omega) - 6\pi R^2\sqrt{-i\omega\rho_f\eta}\,\tilde{v}(\omega) + i\omega\frac{2}{3}\pi R^3\rho_f\tilde{v}(\omega). \tag{3.39}$$

The drag force can be written in the time domain by inverse Laplace transformation, assuming that the bead is at rest for $t \leq 0$ (see Appendix A.2). The resulting force is often called Basset force, to give credit to Basset's work in 1888 [45], however Boussinesq already addressed the problem in 1885 [46]

$$F_{drag}(t) = -6\pi\eta R v(t) - 6R^2\sqrt{\pi\rho_f\eta}\int_0^t \frac{1}{\sqrt{t-t'}}\dot{v}(t')dt' - \frac{2}{3}\pi R^3\rho_f\dot{v}(t). \tag{3.40}$$

The first term in the drag force is the the well known steady state Stokes friction. The second term implies “hydrodynamic memory” of the fluid because of the time integral. As the bead moves, it changes the flow behavior of the fluid around it which will influence the movement of the particle for all future times. Since the memory term is proportional to $\sqrt{\rho_f \eta}$, it can be neglected under certain circumstances such as Brownian motion in air, but certainly not for Brownian motion in water. The last term leads to an added mass in the equations of motion. Descriptive this means, that the effective inertia of the bead is increased because the surrounding fluid has to be displaced too, once the bead is accelerated. Eq. (3.39) can be rewritten as a friction kernel $\gamma[\omega] = -F_{drag}(\omega)/v(\omega)$, introducing a characteristic timescale τ_f which determines when the hydrodynamic effects become important. It reduces to the steady state Stokes friction as $\omega \to 0$

$$\gamma[\omega] = \gamma_s \left(1 + \sqrt{-i\omega\tau_f}\right) - i\omega \frac{2}{3}\pi R^3 \rho_f \tag{3.41}$$

$$\tau_f = \frac{\rho_f R^2}{\eta}. \tag{3.42}$$

Now, one can construct a generalized Langevin equation, replacing the Stokes friction in Eq. (3.33) by the Basset force, assuming that $v(t \leq 0) = 0$ [47]

$$m^* \ddot{x}(t) + 6\pi\eta R \dot{x}(t) + 6R^2 \sqrt{\pi \rho_f \eta} \int_0^t \frac{1}{\sqrt{t - t'}} \ddot{x}(t') dt' + kx(t) = F_{th}(t) \tag{3.43}$$

where m^* is the effective mass of the bead

$$m^* = \frac{4}{3}\pi R^3 \rho_p + \frac{2}{3}\pi R^3 \rho_f \tag{3.44}$$

with particle density ρ_p and fluid density ρ_f. With the added mass, also the Equipartition theorem has to be modified [30, 48]

$$\frac{1}{2}m^*\langle v^2\rangle = \frac{1}{2}k_BT. \tag{3.45}$$

3.3.2 Compressibility effects

Since the incompressible Navier-Stokes equation is the basis for this theory, it does not include compressibility effects. It is expected, that at timescales where the compressibility becomes important, the Equipartition theorem with the bare mass of the particle holds again [48]. This timescale can be estimated by the time which a sound wave needs to propagate by the radius of the bead $\tau_c = R/c \approx 1ns$ which is so small that it cannot be accessed in usual experiments because of the shot noise. Consequently compressibility can be neglected for the purpose of this thesis.

3.3.3 Solving the generalized Langevin equation

The generalized Langevin equation is preferably solved in the frequency domain

$$-i\omega m\tilde{v}(\omega) + \gamma_s\tilde{v}(\omega) + \gamma_s\sqrt{-i\omega\tau_f}\tilde{v}(\omega) - i\omega\frac{2}{3}\pi R^3\rho_f\tilde{v}(\omega) + \frac{k}{-i\omega}\tilde{v}(\omega) = \tilde{F}_{th}(\omega). \tag{3.46}$$

According to Eq. (3.10), the admittance is the linear velocity response to an external force in the frequency domain. It can be found with Eq. (3.46) and

Parameters	$\tau_c = \frac{R}{c}$	$\tau_p = \frac{m}{6\pi R\eta}$	$\tau_f = \frac{\rho_f R^2}{\eta}$	$\tau_k = \frac{6\pi R\eta}{k}$
Silica in water $\rho_p = 2\,g/cm^3$, $\rho_f = 1\,g/cm^3$ $R = 1.5\,\mu m$, $\eta = 10^{-3}\,Pa\,s$ $k_{max} = 100\,\mu N/m$, $k_{min} = 10\,\mu N/m$	$1.1\,ns$	$1\,\mu s$	$2.25\,\mu s$	$0.28\,ms$ $2.8\,ms$

Table 3.1: This table provides an overview over the four characteristic timescales determining Brownian motion in a Newtonian fluid. The timescale of the trap τ_k was computed with the maximum in the experiment accessible trapping strength k and for a weaker strength.

expressed by means of the characteristic timescales and the mass of the particle

$$\mu(\omega) = \frac{\tau_p}{m} \frac{1}{1 - i\omega\tau_p - i\omega\tau_f/9 + 1/(-i\omega\tau_k) + \sqrt{-i\omega\tau_f}}. \tag{3.47}$$

τ_k is yet another characteristic timescale which represents the onset of the trap

$$\tau_k = \frac{\gamma_s}{k}. \tag{3.48}$$

The fluctuation-dissipation theorem Eq. (3.9) connects the admittance to the VACF

$$\tilde{C}_v(\omega) \equiv \int_0^\infty e^{i\omega t} \langle v(t)v(0)\rangle dt = k_B T \mu(\omega). \tag{3.49}$$

Taking the real part on both sides and applying the Wiener-Khinchin theorem Eq. (3.6), yields the velocity PSD

$$S_v(\omega) = 2k_B T \mathrm{Re}\left\{\mu(\omega)\right\} \tag{3.50}$$

and with Eq. (3.8) the position PSD

$$S_x(\omega) = \frac{2k_B T}{\omega^2} \mathrm{Re}\left\{\mu(\omega)\right\}. \tag{3.51}$$

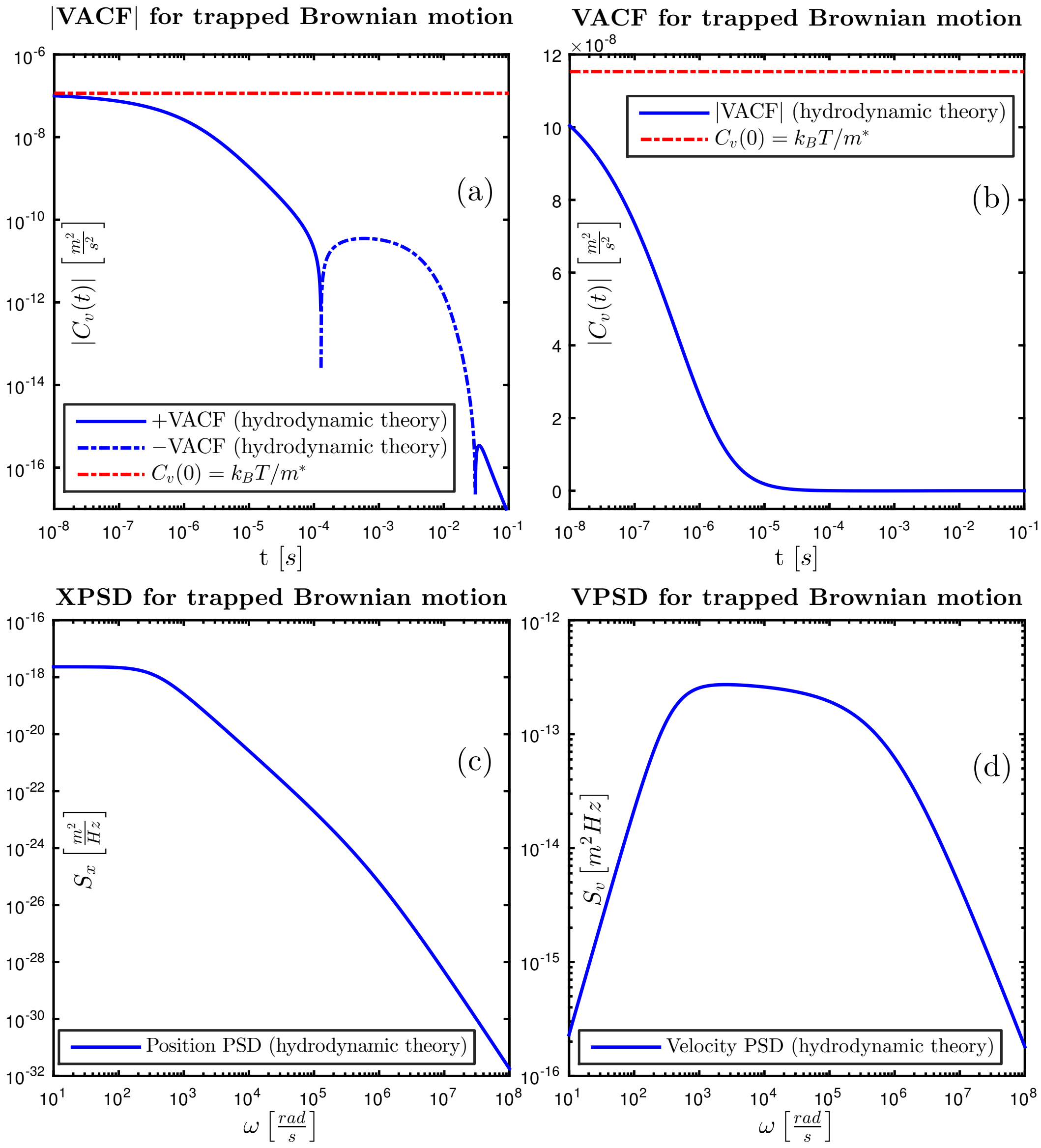

Figure 3.1: All plots of this figure are created with realistic input parameters of silica in water which are listed in Table 3.1 for the weaker trap. (a) and (b) show the VACF in a double- and semi logarithmic plot. In (a), one can see that the VACF is negative (anti-correlated) in a certain time range. This is because of the trap which forces the particle to propagate in opposite direction compared to its initial velocity in order to get back to the trapping center. (c) shows the position power spectral density which flattens for small frequencies because of the trap. (d) shows the velocity power spectral density.

Moreover, the VACF and XACF can be calculated with Eq. (3.7)

$$C_{x/v}(t) = \frac{1}{2\pi} \int_{-\infty}^{\infty} e^{-i\omega t} S_{x/v}(\omega) d\omega. \tag{3.52}$$

Additionally applying the Equipartition theorem leads to the MSD. The relation between the MSD and the XACF is

$$\langle \Delta x^2(t) \rangle = \langle x^2(t) + x^2(0) - 2x(t)x(0) \rangle = 2\langle x^2 \rangle - 2C_x(t) \tag{3.53}$$

with

$$\frac{1}{2} k_B T = \frac{1}{2} k \langle x^2 \rangle \tag{3.54}$$

and consequently, one finds

$$\langle \Delta x^2(t) \rangle = \frac{2k_B T}{k} - \frac{2}{\pi} \int_{0}^{\infty} \cos(\omega t) S_x(\omega) d\omega. \tag{3.55}$$

An analytical solution for the PSD can easily be found with the admittance given in Eq. (3.47). The transformation back to the time domain to obtain the VACF and MSD according to Eq. (3.52), however, is nontrivial. Analytic solutions were found by Clercx and Schram and are listed in Appendix A.4.

3.3.4 Colored thermal force

The thermal force which corresponds to the generalized Langevin equation is colored which means that it is not delta-correlated any more. The thermal force PSD can be calculated with the fluctuation-dissipation theorem Eq. (3.12)

$$S_{F_{th}}(\omega) = 2k_B T \gamma_s \left(1 + \sqrt{\frac{|\omega| \tau_f}{2}}\right) \tag{3.56}$$

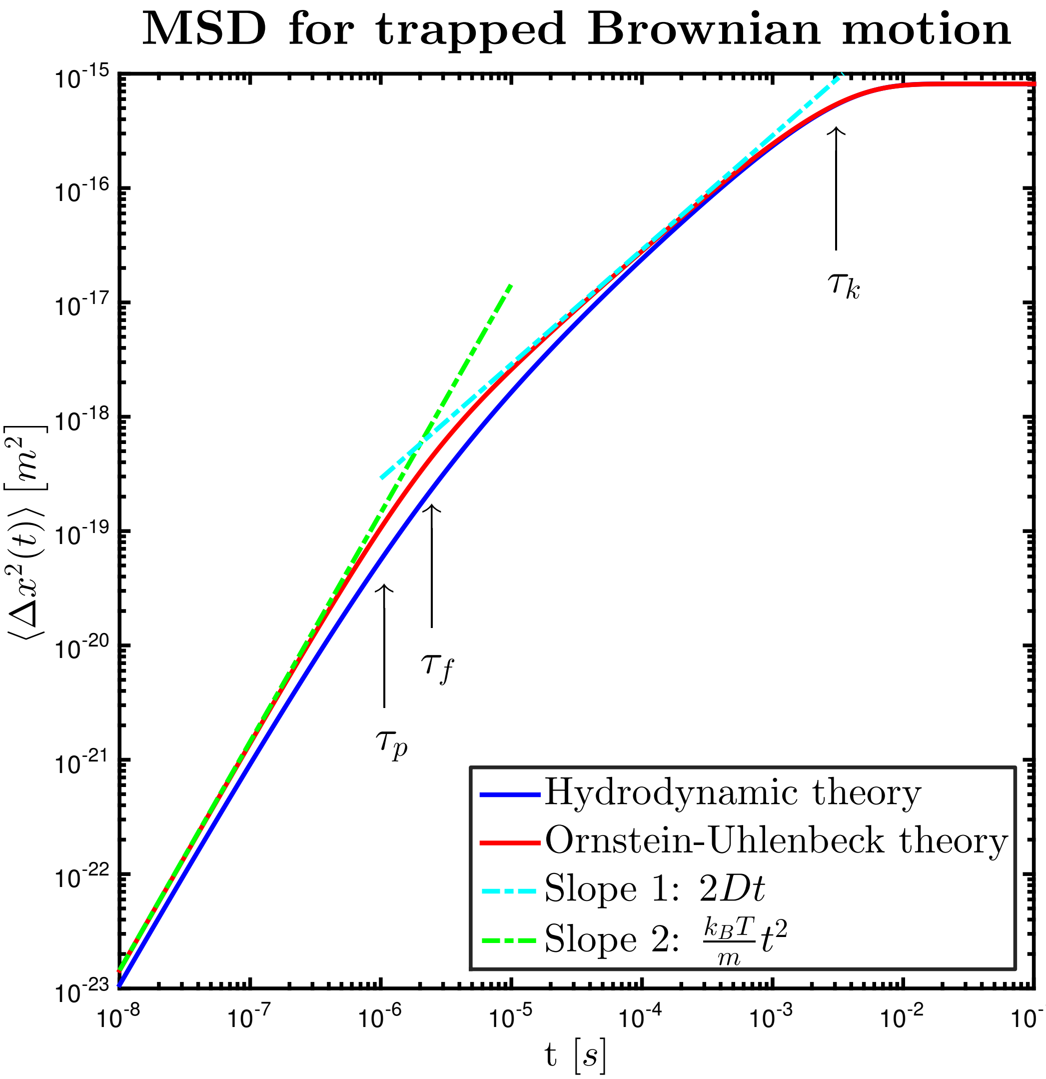

[h]

Figure 3.2: Mean square displacement for silica in water with input parameters of Table 3.1 for the weaker trap. The graphic shows the differencecs between the Ornstein-Uhlenbeck theory and the hydrodynamic theory which are severest around $t \approx \tau_f$. For $t \ll \tau_p$ the motion is in the ballistic regime, where the theories don't match because the hydrodynamic theory is proportional to $\frac{k_B T}{m^*} t^2$ rather than $\frac{k_B T}{m} t^2$. For the hydrodynamic theory, the diffusive, long time regime is barely reached because of the trap.

The thermal force correlation is then obtained with the Wiener-Khinchin theorem Eq. (3.7)

$$C_{F_{th}}(t) = 2k_B T \gamma_s \left(\delta(t) - \frac{1}{4}\sqrt{\frac{\tau_f}{\pi}} |t|^{-3/2} \right). \tag{3.57}$$

The thermal force has compared to the Ornstein-Uhlenbeck theory a long time $|t|^{-3/2}$ correlation, which corresponds to the hydrodynamic memory of the fluid.

3.4 Brownian motion in complex fluids

The dynamic viscosity η as it is found in the Navier Stokes equation can be defined with Couette flow. A layer of fluid is trapped between two large plates where one of them is at rest and the other is moving with a constant speed v. The velocity of the fluid field decays linearly in a laminar flow form v at the moving plate to zero at the steady plate. Because of the viscosity of the fluid, there is a force on the plate in opposite direction of its movement

$$F = \eta \frac{A}{d} v. \tag{3.58}$$

This definition goes back to Newton in 1687. Eq. (3.58) can be rewritten in terms of the stress $\sigma = F/A$ and strain rate $\dot{\gamma} = v/d$, where A is the area of each plate and d is their distance [49]

$$\sigma(t) = \eta \dot{\gamma}(t). \tag{3.59}$$

The Newtonian fluid responds instantaneously to shear with an irreversible

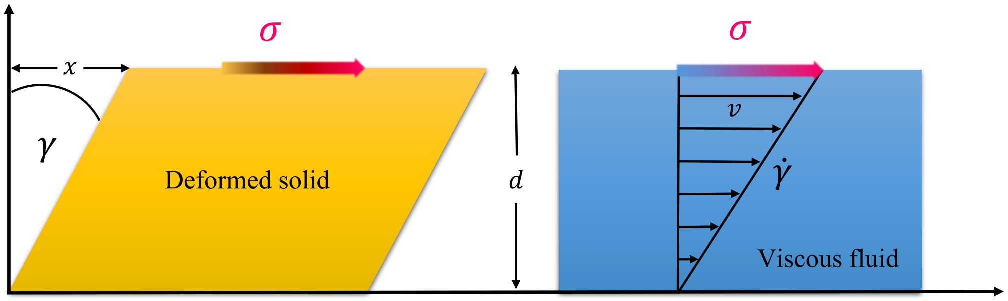

Figure 3.3: Illustration of stress and strain for an elastic solid and a viscous fluid. For Couette flow, the strain rate is constant. In general, however, it is time dependent.

deformation. An elastic solid is usually modeled with Hooke's Law (1678) where the stress is proportional to the strain $\gamma = x/d$. The constant of proportionality is called shear modulus G [49]

$$\sigma(t) = G\gamma(t). \tag{3.60}$$

In this case, the solid also responds instantaneously to shear, but the deformation is fully reversible. In reality, there is no such thing as a purely viscous fluid. All fluids contain elastic elements which lead to a delayed response, it just depends on the timescale where these become important. For water e.g. this timescale is $\tau_w \approx 10^{-12}\,s$, and so it acts as a Newtonian fluid in usual experiments [49]. The viscoelastic impact is likely to become more important for fluids composed of larger molecules such as polymers.

Linear viscoelasticity can be expressed with the complex shear modulus $G^*(\omega)$ which is the response function between stress to and strain in the frequency domain.

$$\sigma(\omega) = G^*(\omega)\gamma(\omega) \tag{3.61}$$

with

$$G^*(\omega) = G'(\omega) - iG''(\omega). \tag{3.62}$$

$G'(\omega)$ is called storage modulus because it represents the elastic part which stores potential energy and $G''(\omega)$ as loss modulus takes the viscous, dissipating part into account. Equivalently one can define a complex viscosity relating stress and strain rate in frequency domain

$$\sigma(\omega) = \eta(\omega)\dot{\gamma}(\omega). \tag{3.63}$$

Since $\dot{\gamma}(\omega) = -i\omega\gamma(\omega)$, the complex shear modulus $G^*(\omega)$ and the complex viscosity $\eta(\omega)$ are related with

$$\eta(\omega) = \frac{G^*(\omega)}{-i\omega}. \tag{3.64}$$

For a purely viscous fluid, such as water, except at very short timescales, the complex viscosity is purely real and constant. For an ideal, elastic solid, the complex viscosity is purely imaginary and constant.

3.4.1 Extension of the hydrodynamic theory

In order to study Brownian motion in complex fluids, the previous theory is still applicable, when replacing the constant viscosity η by the frequency dependent complex viscosity $\eta(\omega)$ [12, 50]. In this case it is convenient to express the complex viscosity with a dimensionless function

$$\psi(\omega) = \frac{\eta(\omega)}{\eta(0)}. \tag{3.65}$$

The characteristic timescales are then defined with the steady state viscosity

$$\tau_p \equiv \frac{m}{6\pi\eta(0)R} \tag{3.66}$$

$$\tau_f \equiv \frac{\rho_f R^2}{\eta(0)}. \tag{3.67}$$

In this case, the admittance is given by

$$\mu(\omega) = \frac{\tau_p}{m} \frac{1}{\psi(\omega) - i\omega\tau_p - i\omega\tau_f/9 + 1/(-i\omega\tau_k) + \sqrt{\psi(\omega)}\sqrt{-i\omega\tau_f}}. \tag{3.68}$$

3.4.2 The Maxwell model

A very simple model for a complex fluid was proposed by Maxwell in 1867 [50]. It consists of a viscous element with steady state viscosity $\eta_0 = \eta(\omega = 0)$ and an infinite frequency shear modulus $G_\infty = G^*(\omega = \infty)$, such that their strains add $\gamma(t) = \gamma_{G_\infty}(t) + \gamma_{\eta_0}(t)$. Consequently, one finds

$$\dot{\gamma}(t) = \frac{1}{G_\infty}\dot{\sigma}(t) + \frac{1}{\eta_0}\sigma(t). \tag{3.69}$$

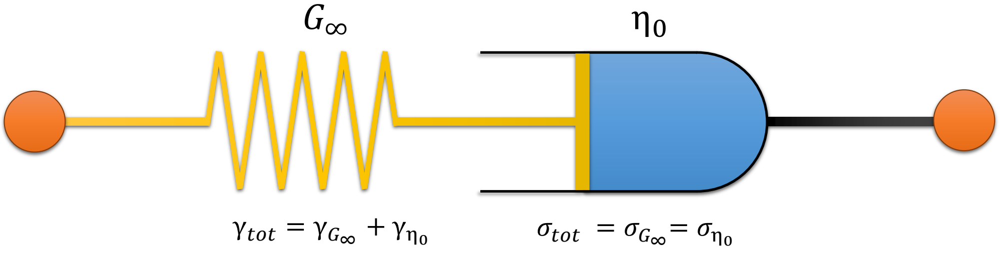

Figure 3.4: The Maxwell model consists of a purely elastic spring and a purely viscous dashpot which are connected in series. While the stress is the same in the whole element, strains of the elastic and viscous parts add.

Fourier transform yields the complex shear modulus

$$G^*(\omega) = \frac{\omega^2\tau_m^2 G_\infty}{1+\omega^2\tau_m^2} - i\frac{\omega\tau_m G_\infty}{1+\omega^2\tau_m^2} \tag{3.70}$$

where $\tau_m = \eta_0/G_\infty$ is called Maxwell time and characterizes the timescale where elasticity becomes important. The PSD of Brownian motion in a Maxwell fluid can be obtained analytically. The transformation back to time domain, however, is done numerically with a Filon algorithm [51]. To make complex fluid models more realistic, additional parameters can be introduced. One can for example add a background viscosity η_∞ to the complex viscosity in order to prevent the behavior of vanishing viscosity as $\omega \to \infty$ in the Maxwell model. A more thorough discussion of Brownian motion in a Maxwell fluid has been done by Grimm et al. [50].

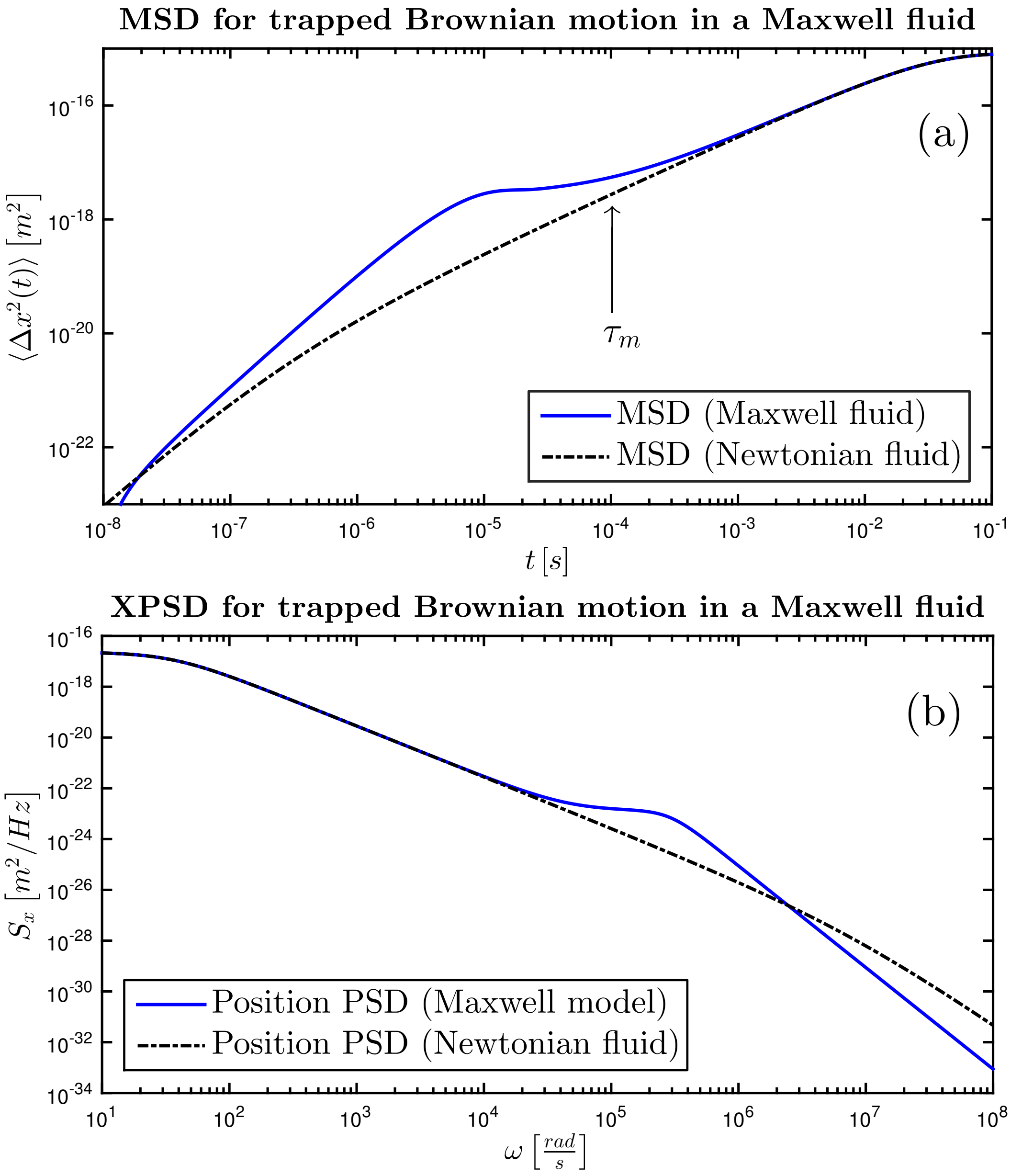
MSD for trapped Brownian motion in a Maxwell fluid

XPSD for trapped Brownian motion in a Maxwell fluid

Figure 3.5: Both plots have been calculated with the parameters of Table 3.1, except $\eta_0 = 10\,\eta_{water}$ and $\tau_m = 10^{-4}\,s$. The MSD (a) has a plateau around the resonance time $t = \tau_m$ which hinders the particle propagation because of the elastic component of the fluid, similarly to the optical trap. The position PSD (b) has a plateau along with the MSD.

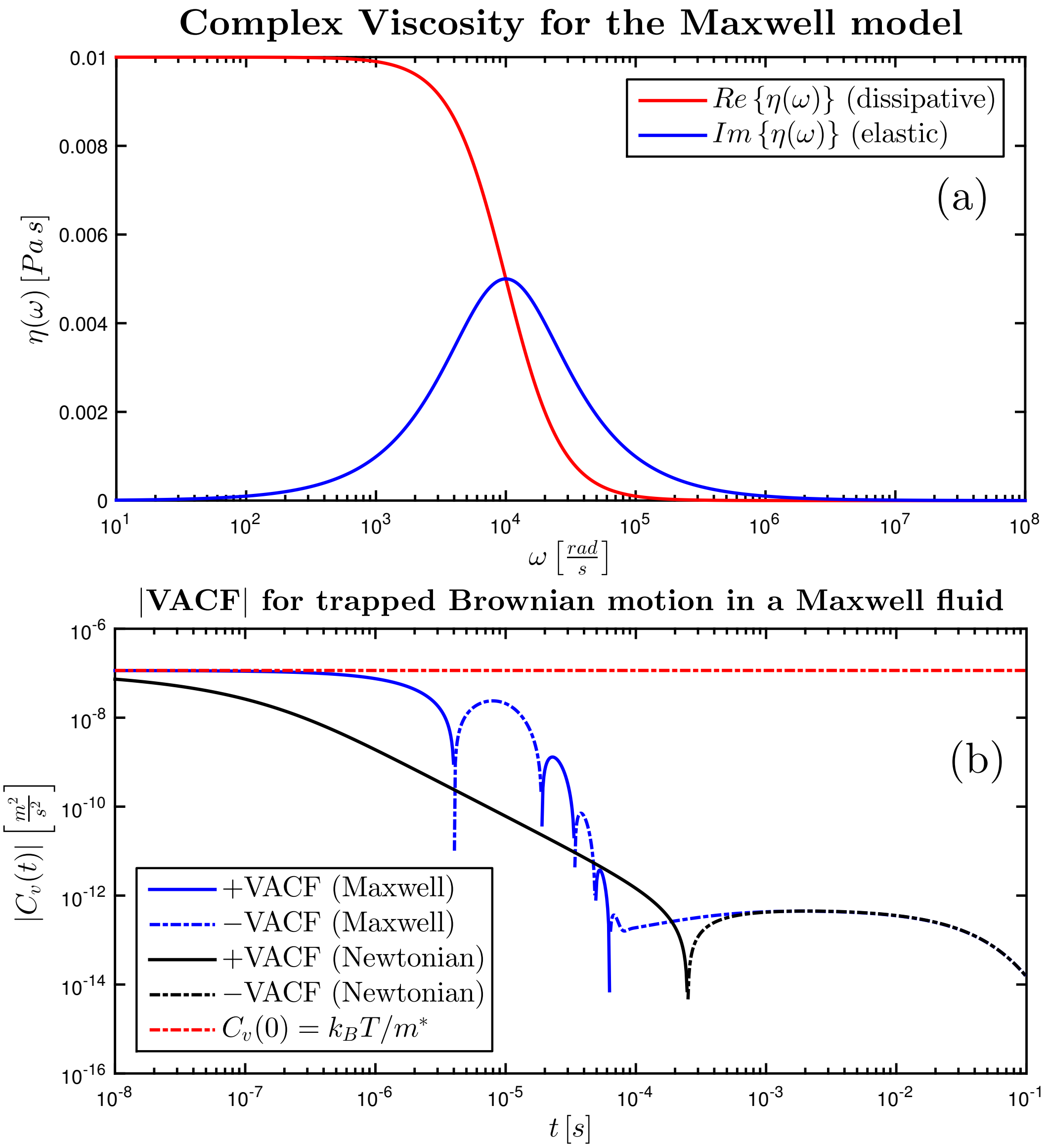

Figure 3.6: Both plots have been calculated with the parameters of Table 3.1, except $\eta_0 = 10\,\eta_{water}$ and $\tau_m = 10^{-4}\,s$. The real part of the viscosity (a) decreases for increasing angular frequency which is called shear thinning and is indeed observed in many complex fluids. The elastic part of the viscosity has its maximum at $\omega = 1/\tau_m$ and can be understood as a resonance frequency of the complex fluid. The VACF (b) has additional zero crossings which can be understood as an effect of the elasticity which makes the velocity change its direction at certain timescales.

3.5 Estimating viscoelastic moduli from the observation of Brownian motion

This section explains how to calculate the complex viscosity from measurable quantities of Brownian motion. The standard method to do that was proposed by Mason and Weitz in 1995 [10], which is however not accurate at high frequencies. The following deduces the exact formula, relating the complex viscosity to the MSD and discusses the limitations of the method, concluding that the choice of an appropriate Laplace transformation algorithm is substantial to obtain correct results at high frequencies.

3.5.1 Accounting for hydrodynamic effects

The formula which Mason and Weitz initially proposed to calculate the complex viscosity from the MSD is [10, 52–54]

$$\eta(s) = \frac{k_B T}{\pi R s^2 \langle \Delta \tilde{x}^2(s) \rangle} - \frac{ms}{6\pi R} \tag{3.71}$$

where $\langle \Delta \tilde{x}^2(s) \rangle$ denotes the Laplace transform of the MSD

$$\langle \Delta \tilde{x}^2(s) \rangle = \int_0^\infty e^{-st} \langle \Delta x^2(t) \rangle dt \tag{3.72}$$

with $s = -i\omega$ in the convention of this thesis. Eq. (3.71) can easily be extended to trapped Brownian motion [55]

$$\eta(s) = \frac{k_B T}{\pi R s^2 \langle \Delta \tilde{x}^2(s) \rangle} - \frac{ms}{6\pi R} - \frac{k}{6\pi R s}. \tag{3.73}$$

This theory is based on the friction kernel $\gamma[\omega] = 6\pi R \eta(\omega)$ which corresponds to the Ornstein-Uhlenbeck theory of Brownian motion. Consequently it is only valid when hydrodynamic effects which mostly affect the high frequency behavior are negligible. In order to get the hydrodynamic counterpart, one has solve Eq. (3.49) with the admittance given in Eq. (3.68) for $\eta(\omega)$ which has been done by Felderhof in 2011 [12]

$$\eta(\omega) = \eta_0 \left[\sqrt{\frac{k_B T}{m} \frac{\tau_p}{\tilde{C}_v(\omega)} + \frac{1}{i\omega\tau_k} + i\omega \left(\tau_p - \frac{5}{36}\tau_f \right)} - \frac{1}{2}\sqrt{-i\omega\tau_f} \right]^2 . \quad (3.74)$$

Eq. (3.74) can be rewritten in terms of the MSD, using [53]

$$\langle \Delta\tilde{x}^2(\omega) \rangle = -\frac{2}{\omega^2} \tilde{C}_v(\omega) \qquad \text{for} \quad \omega \neq 0 \quad (3.75)$$

which is proven in Appendix A.3, resulting in

$$\eta(\omega) = \eta_0 \left[\sqrt{-\frac{2k_B T}{m} \frac{\tau_p}{\omega^2 \langle \Delta\tilde{x}^2(\omega) \rangle} + \frac{1}{i\omega\tau_k} + i\omega \left(\tau_p - \frac{5}{36}\tau_f \right)} - \frac{1}{2}\sqrt{-i\omega\tau_f} \right]^2 . \quad (3.76)$$

Taking the limit $\omega\tau_f \to 0$, Eq. (3.76) reduces to Eq. (3.73) which confirms the compatibility with the Mason-Weitz method if hydrodynamic effects are negligible or frequencies are sufficiently low. Note, that the MSD varies by a factor of three, because Mason's theory is based on a three dimensional trajectory and the theory in this thesis is one dimensional $\langle \Delta\mathbf{x}^2(t) \rangle_{3D} = 3\langle \Delta x^2(t) \rangle_{1D}$. Figure 3.7 shows, that the Mason-Weitz formula with theoretical water data and realistic input parameters is sufficient to $\omega \approx 10^4\, rad/s$. This limit, however, depends highly on the input parameters and shifts especially for smaller bead radii and higher fluid viscosities to higher angular frequencies. Consequently, Eq. (3.73) may still be valid for many complex fluids up to even higher frequencies.

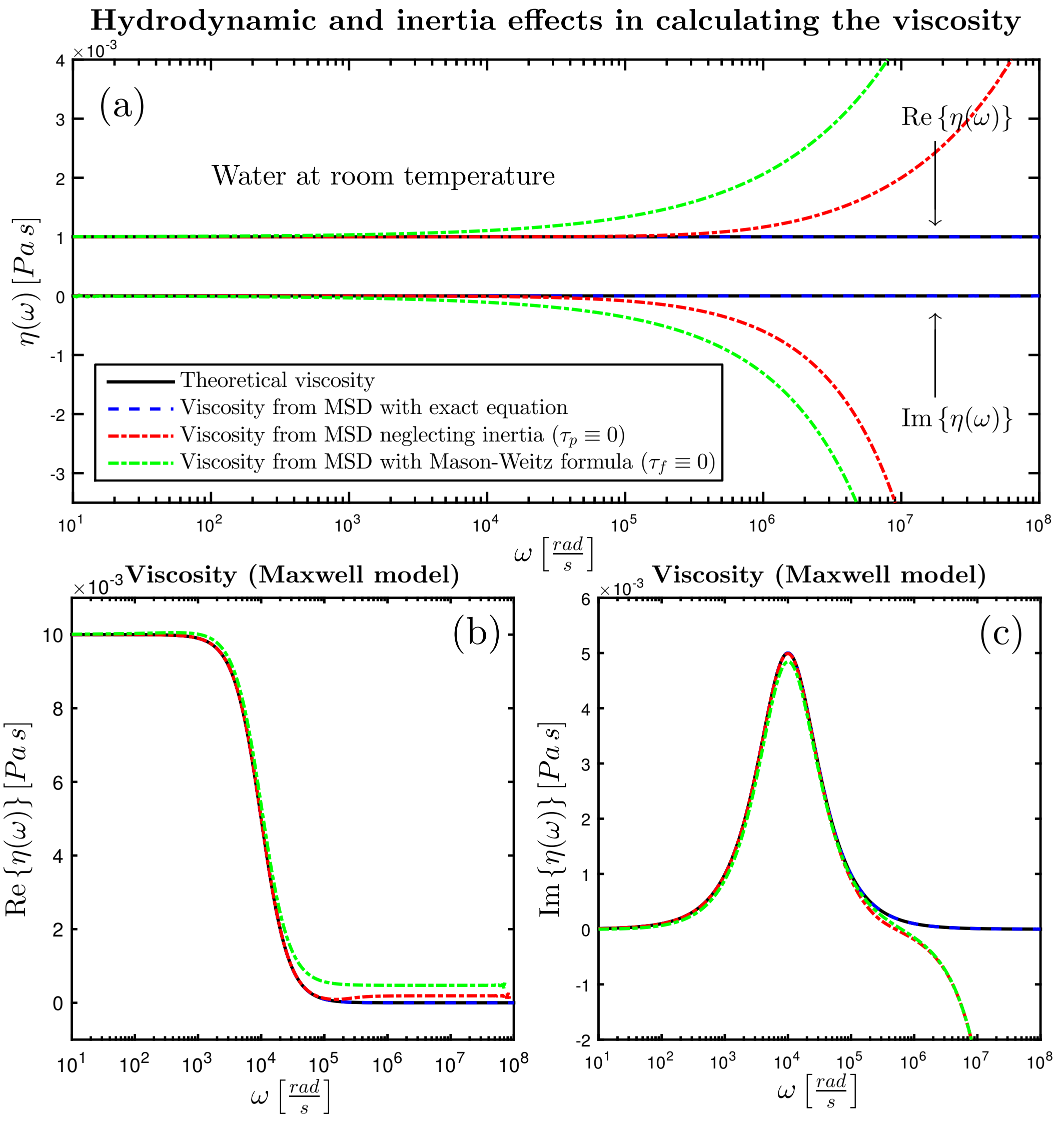

Figure 3.7: This figure shows the results of the complex viscosity calculated from the hydrodynamic MSD (Eq. (A.24)). The input parameters are the same as in Figure 3.2 and Figure 3.5 except this time the stronger trap $k = 10^{-4}\,N/m$ is assumed. (a) shows the result for water, (b) and (c) show the results for the Maxwell model. The exact formula Eq. (3.76) is capable of giving the correct result over the whole frequency window. Neglecting inertia or hydrodynamics causes deviations at high frequencies.

3.5.2 Limitations of the method

The main limitation to reach high frequencies is the sampling frequency of the MSD data or the time window where the MSD is known. The Nyquist-Shannon sampling theorem states [56]:

> "If a function $f(t)$ contains no frequencies higher than W cps, it is completely determined by giving its ordinates at a series of points spaced $1/2W$ seconds apart."

Consequently one cannot obtain any frequency information from a time signal for $f > f_s$ where

$$f_s = \frac{1}{2\Delta t} \tag{3.77}$$

is the Nyquist frequency and Δt is the time increment between two points of an equally spaced signal. The Laplace transform above that frequency is artificial and unfortunately these artefacts almost surely also affect the desired region below the Nyquist frequency due to interpolation errors [1]. This effect can be minimized by oversampling and optimizing the interpolation scheme of the Laplace transform algorithm.

For Brownian motion, the smallest time where the MSD can be measured is determined through shot noise. For the detection system described in section 2.2, it is $t_{min} \approx 100\,ns$ which yields the Nyquist freqnency $f_s \approx 5$MHz. The fastest possible acquisition rate is 200 MHz. Figure 3.8 shows the results of the viscosity calculated with the exact formula for theoretical predictions of the MSD with realistic water input parameters for different algorithms. The algorithm proposed by Evans et al. [57] extrapolates the input function linearly between each two points and analytically solves these integrals to obtain the Laplace transform. Moreover, the input function is extrapolated to zero and infinity. The parabolic analytic algorithm does the same, except interpolating each three points as a parabola rather than linear interpolating. The parabolic algorithm comes closest to the Nyquist limit and is discussed in detail in Appendix C.

Further sources of error are random deviations and noise, which always occur since the statistical quantities are defined for an average over infinite time which is of course impossible in practice. One can reduce this effect, by data binning, which means averaging over a set of points and replace them by its mean value which is also desirable in regards of computation time. Figure 3.9 shows the result for the calculated viscosity where the number of data points of the input MSD has been reduced from around two million to 1000 by binning. The outcome for the parabolic algorithm is almost unchanged while the linear algorithm fails at a much lower frequency compared to Figure 3.8.

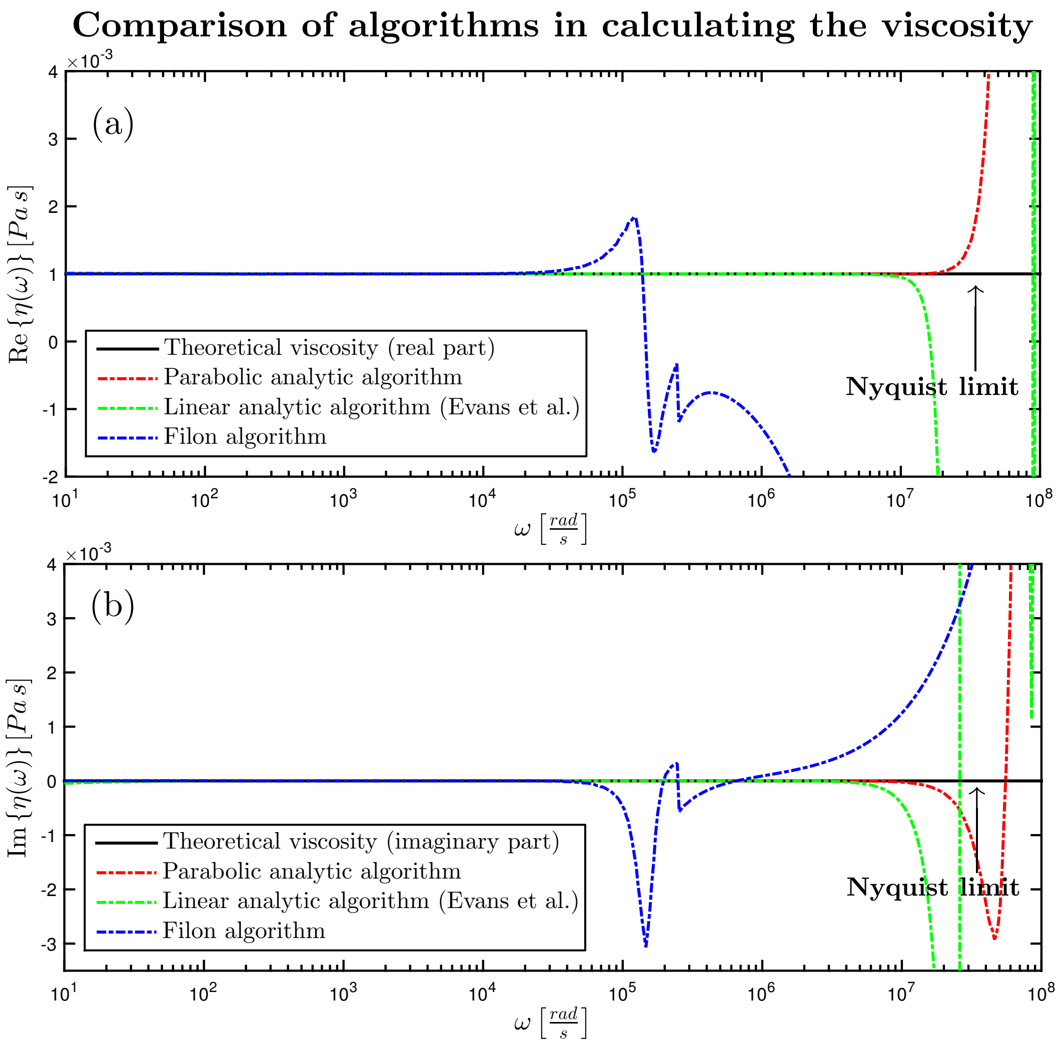

Figure 3.8: This figure shows the viscosity calculated from the theoretical hydrodynamic MSD (Eq. (A.24)). The input parameters are realistic for what can be achieved in the experiment to give theoretical predictions for the data analysis. The time window in which the input MSD is given, is $100\,ns < t < 0.01\,s$. The data points are equally spaced in time with the oversampled maximum achievable sampling rate of 200 MSa/s to minimize interpolation errors. The Laplace transform of the MSD is calculated with different algorithms, pointing out that the parabolic algorithm produces the best results.

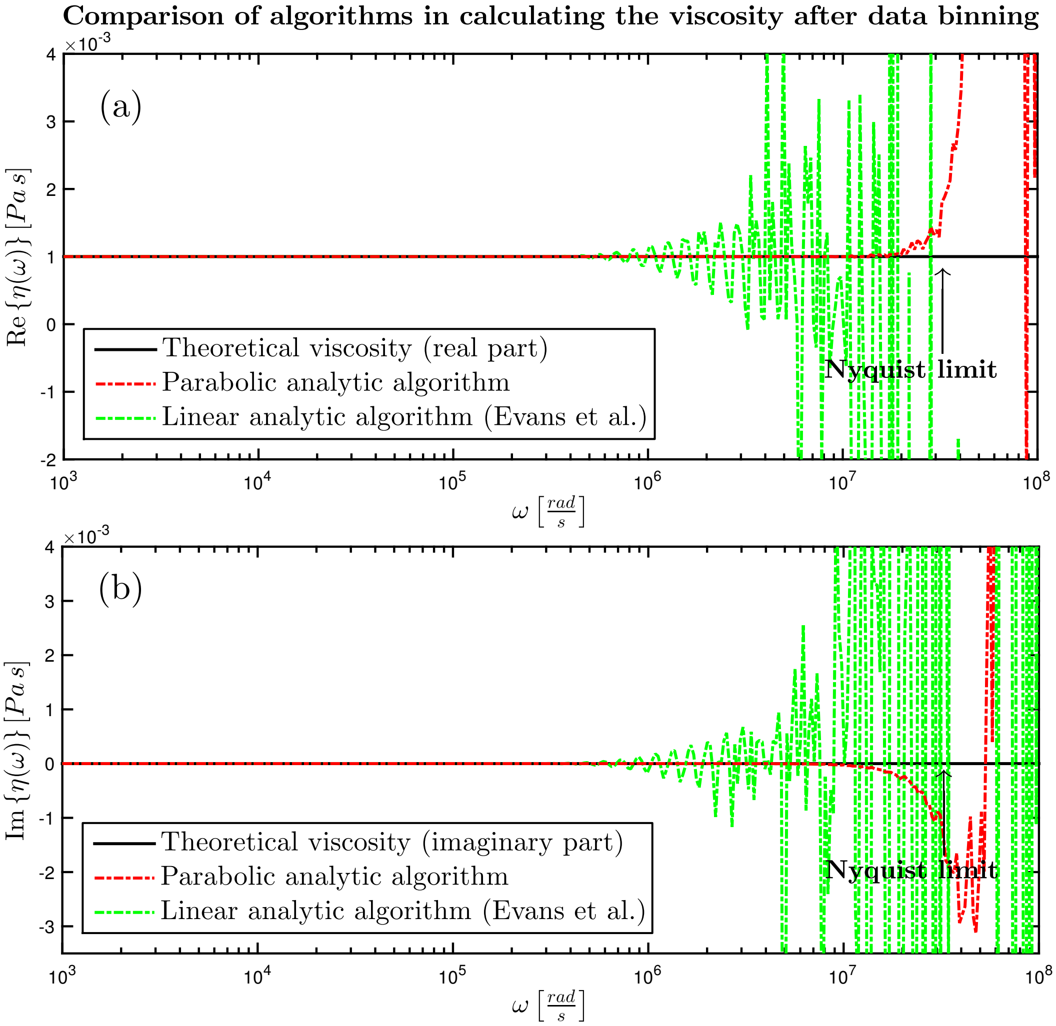

Figure 3.9: The input parameters of this plot are the same as in Figure 3.8. However, the number of input data points of the MSD has been reduced from around two million to one thousand by data bining. By doing this, one can reduce the noise in real data and achieve a much shorter computation time. While the linear algorithm fails at much lower frequency, the results of the parabolic algorithm are almost the same as before binning which makes it favorable for real data.

Chapter 4

Data analysis and results

This chapter explains how to analyze Brownian motion data in order to obtain the complex viscosity. It contains an optimization of the algorithm, data fitting and dealing with noise. Afterwards, the results for water and acetone will be presented in very good agreement with the theory. Finally there is an outlook how to apply the method to complex fluids.

4.1 Optimizing the algorithm

The experimental data input in order to obtain the complex viscosity is the Laplace transform of the VACF or MSD. Figure 4.1 shows that the VACF is very sensitive to noise and it is consequently advantageous to use the MSD and Eq. (3.76) to obtain the complex viscosity. However, it turns out that the data analysis can be further improved by applying the following decomposition instead of calculating the Laplace transform of the MSD directly.

$$\langle \Delta \tilde{x}^2(s) \rangle = \int_0^\infty e^{-st} \left(\frac{2k_BT}{k} - 2C_x(t) \right) dt = \frac{2k_BT}{ks} - 2\int_0^\infty e^{-st} C_x(t) dt \quad (4.1)$$

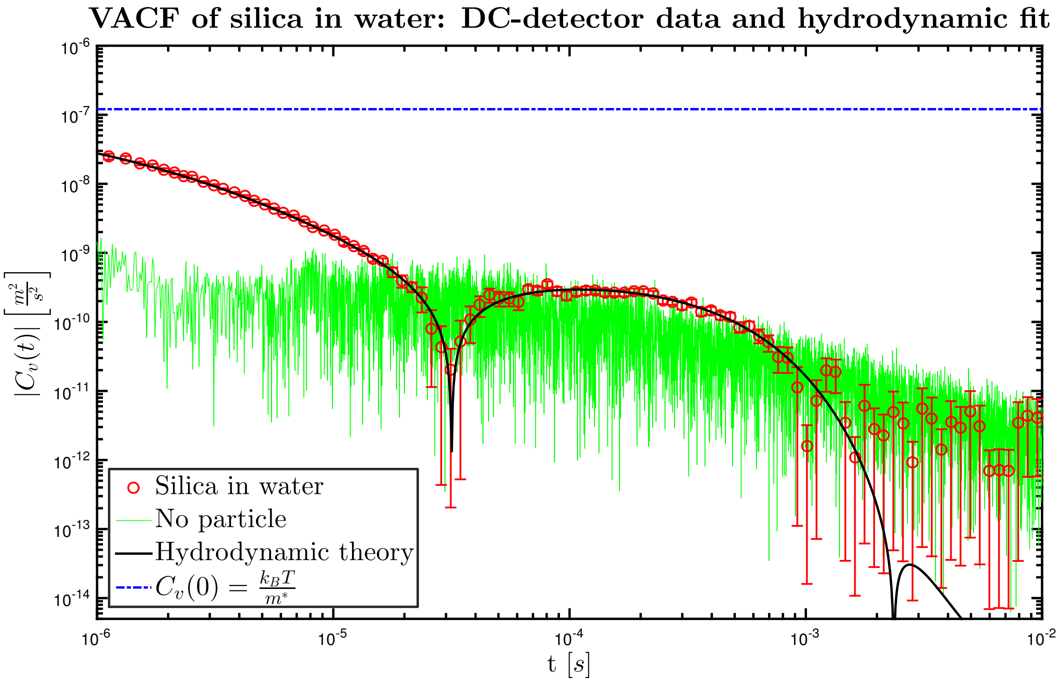

Figure 4.1: The VACF of a Brownian particle is much more noisy than the MSD and thus disadvantageous to use in data analysis.

$$\begin{aligned} \langle \Delta\tilde{x}^2(\omega)\rangle &= \frac{i}{\omega}\frac{2k_BT}{k} - 2\int_0^\infty \cos(\omega t)\, C_x(t)dt - \mathrm{Im}\left\{\mathcal{L}_t\left\{2C_x(t)\right\}\right\} \\ &= \frac{i}{\omega}\frac{2k_BT}{k} - S_x(\omega) - \mathrm{Im}\left\{\mathcal{L}_t\left\{2C_x(t)\right\}\right\}. \end{aligned} \tag{4.2}$$

Eq. (4.2) improves the quality of the real part of $\langle \Delta\tilde{x}^2(\omega)\rangle$ because the PSD can be determined with less numerical effort and error propagation then the Laplace transform of the XACF which is relevant at high frequencies as confirmed in Figure 4.2 for real data.

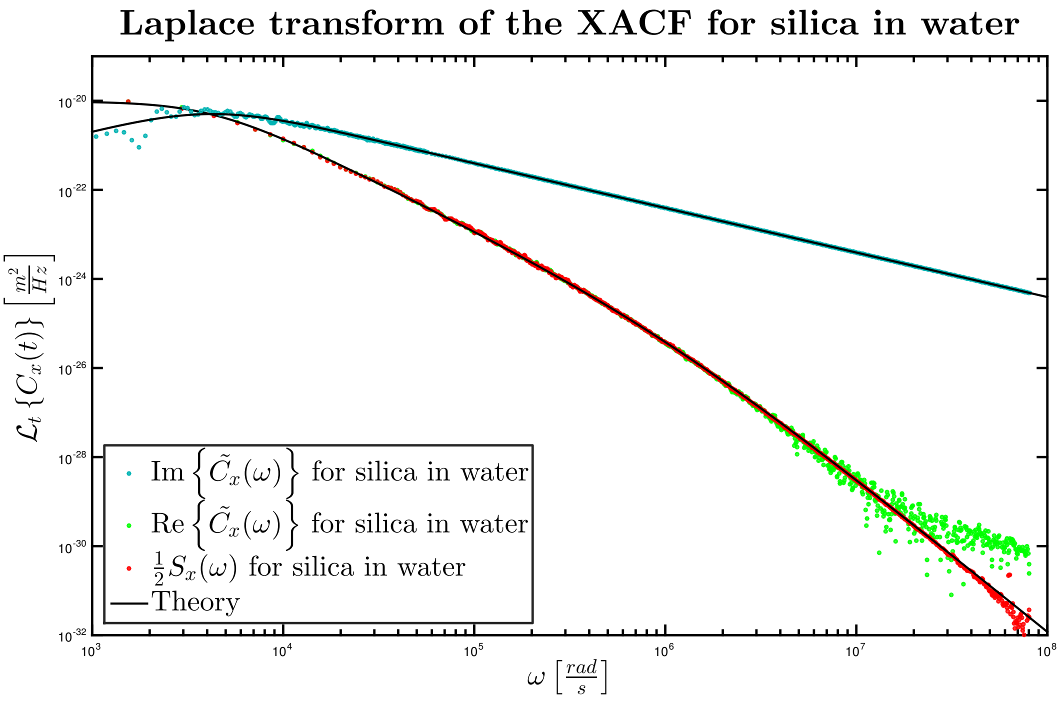

Figure 4.2: The imaginary part seems to fit very well to the theory. This is because the high frequency behavior is mostly determined by the extrapolation of the XACF to $t = 0$ which is incorporated in the Laplace transform algorithm. It consequently is highly dependent on the fitting parameters. As one can see, the real part can be determined much more accurately with the position PSD because it produces less numerical errors.

4.2 Parameter fitting

Since the output of the split beam detection system is a voltage $V(t) = x(t)C_{V/m}$, the calibration constant $C_{V/m}$ is determined by least squares fitting to the hydrodynamic theory. Another fitting parameter is the radius of the bead. The trapping constant k, however, is not an independent fitting parameter since it is related to the volts to meter calibration constant by the

Maxwell Boltzmann distribution [58]

$$P(x) \propto e^{-kx^2/k_BT} \tag{4.3}$$

and the Equipartition theorem

$$\frac{1}{2}k\langle x^2\rangle = \frac{1}{2}k_BT \quad \Leftrightarrow \quad C_{V/m} = \sqrt{\frac{k\langle V^2\rangle}{k_BT}}. \tag{4.4}$$

For the fit, the number of data points has been reduced to around 200 by data binning.

4.3 Detection noise

The accessible frequency range of the signal is limited by photon shot noise at high frequencies. The low frequency behavior is disturbed by physical vibration of the optics and the resulting noise. This section explains how to minimize these effects in terms of data analysis.

4.3.1 Shot noise

The measured displacement is a sum of the real position of the particle plus detection noise $x_{msr}(t) = x_p(t) + x_n(t)$. The measured MSD is [59]

$$\begin{aligned}\langle \Delta x^2(t)\rangle_{msr} &= \langle [x_{msr}(t) - x_{msr}(0)]^2\rangle \\ &= \langle [x_p(t) - x_p(0)]^2\rangle - \langle [x_n(t) - x_n(0)]^2\rangle \\ &+ 2\langle [x_p(t) - x_p(0)]\,[x_n(t) - x_n(0)]\rangle \\ &\approx \langle \Delta x^2(t)\rangle_p - \langle \Delta x^2(t)\rangle_n.\end{aligned} \tag{4.5}$$

The correlation between the particle position and the detection noise can be neglected at short times where the uncorrelated photon shot noise is dominant. Consequently the particle MSD can be obtained by subtracting a noise measurement without a bead from the measured data. The same is true for the particle PSD. The shot noise in the PSD is flat (independent of ω), which also leads to a flat noise for the MSD at short times since

$$\begin{aligned}\langle \Delta x^2(t)\rangle_n &= 2\langle x_n^2\rangle - 2\langle x_n(t)x_n(0)\rangle \approx 2\langle x_n^2\rangle - \frac{1}{\pi}\int_{-\infty}^{\infty} e^{-i\omega t} S_{Shot} d\omega \\ &= 2\langle x_n^2\rangle - 2S_{Shot}\delta(t) = const. \quad \text{for } t \neq 0.\end{aligned} \tag{4.6}$$

More accurate then using a noise measurement is to implement the shot noise as an additional fitting parameter to subtract it from the signal afterwards

$$S_{x,fit}(\omega) = S_{x,theory}(\omega) + S_{Shot} \tag{4.7}$$

$$S_{x,p}(\omega) = S_{x,msr} - S_{Shot} \tag{4.8}$$

$$\langle \Delta x^2(t)\rangle_{fit} = \langle \Delta x^2(t)\rangle_{theory} + \langle x^2\rangle_{Shot} \tag{4.9}$$

$$\langle \Delta x^2(t)\rangle_{p} = \langle \Delta x^2(t)\rangle_{msr} - \langle x^2\rangle_{Shot}. \tag{4.10}$$

4.3.2 Low frequency noise

Low frequency noise cannot be eliminated in the same way as shot noise, because it is correlated to the motion. Instead, the vibration noise peaks can be artificially flattened since the low frequency PSD is known to be constant because of the trap. Low frequency noise also affects the root mean square

$\langle x^2 \rangle$ which is why the MSD is determined with the following calibration:

$$\begin{aligned}\langle [V(t) - V(0)]^2 \rangle_{msr} &= 2\langle V^2 \rangle_{msr} - 2\langle V(t)V(0) \rangle_{msr} \\ &= \frac{1}{\pi} \int_{-\infty}^{\infty} \left[e^{-i\omega 0} - e^{-i\omega t} \right] P_V(\omega) d\omega\end{aligned} \tag{4.11}$$

Since the mechanical vibration noise is only dominant at low frequencies ($f \lesssim 500\,Hz$), Eq. (4.11) produces correct results for sufficiently small times because the low frequency behavior mostly cancels out. In order to obtain the full MSD, it is first computed at an sufficiently small calibration point t_c. Afterwards, the PSD is artificially flattened at $f = f_{flat}$ and the XACF is calculated with

$$C_V(t) = \frac{1}{2\pi} \int_{-\infty}^{\infty} e^{-i\omega t} P_{V,flat}(\omega) d\omega \tag{4.12}$$

The root mean square can then be determined with the calibrated MSD

$$\langle V^2 \rangle = \frac{1}{2} \langle \Delta V^2(t_c) \rangle_{msr} + C_V(t_c) \tag{4.13}$$

and one can conclude to the full MSD

$$\langle \Delta V^2(t) \rangle = 2\langle V^2 \rangle - 2C_V(t). \tag{4.14}$$

This procedure of course leads to a systematical error at large times and doesn't contain real information for $t \gtrsim 1/f_{flat}$.

4.4 Results

This section presents the microrheological results for water and acetone. These Newtonian fluids have been chosen in order to verify the theory and data analysis procedure because their viscosity is known to be constant with vanishing imaginary part. The experiment was performed using silica beads (Bangs Labratories, n=1.46, ρ=2.0 g/cm^3) at $T = 22 \pm 1°C$ in HPLC-grade water (n=1.33, ρ=0.998 g/cm^3, η_0=9.55 $\times 10^{-4}\,Pa\,s$) and HPLC-grade acetone (n=1.35, ρ=0.789 g/cm^3, $\eta_0 = 3.17 \times 10^{-4}\,Pa\,s$). The DC-detector data was collected with a sampling rate of 25 MSa/s whereas the AC-detector data was acquired with the maximum available sampling rate of 200 MSa/s. A single data set contains 2^{27} points which yields a recording time of around 5.3 s for the DC-detector and 0.67 s for the AC-detector.

The data analysis has been done with MATLAB. The Fourier transformation to obtain the PSD has been computed with the in-built Fast Fourier Transform algorithm and Laplace transformations were calculated with the algorithm derived in Appendix C.

4.4.1 DC-detector results

Table 4.1 lists mean values of the fitting parameters determined from many independent data sets of the same bead respectively. For the DC-data, the trapping power has been doubled after each measurement cycle. The fitted trapping strength k also doubles with the laser power, which confirms the correctness of the fit. The third trapping strength corresponds to the maximum available laser power which is approximately 300 mW at the trapping center. With increasing trapping power, the detection power could also be increased to a maximum of $P \approx 2\,mW$ because the mobility of the bead is reduced and the maximum peak to peak voltage is reached at a higher detection power. Accordingly, the shot noise level decreases.

Figure 4.3 shows the fit of the MSD and PSD for a data set with maximum trapping power. The PSD was typically flattened at $140\,Hz$ to avoid the strong $120\,Hz$ noise peak. For lower trapping power, the noise effects were less severe and flattening was not necessary or shifted to lower frequencies. Figure 4.4 shows the result for the complex viscosity which is in very good agreement with the expected constant real part and vanishing imaginary part for a Newtonian fluid. The frequency range where the method produces correct results is mainly determined by the time window where the MSD is know and yields $\omega_{max} \approx 10^6\,rad/s$ for the DC-detector.

$C_{V/m}$	k_{trap}	$\sqrt{S_{Shot}}$	R
Silica in water DC-detector			
$12.5 \pm 0.3\,mV/nm$	$25 \pm 1\,\mu N/m$	$90.4 \pm 1.6\,fm/\sqrt{Hz}$	$1.53 \pm 0.04\,\mu m$
$24.9 \pm 0.4\,mV/nm$	$49 \pm 2\,\mu N/m$	$59.8 \pm 2.0\,fm/\sqrt{Hz}$	
$48.5 \pm 1.1\,mV/nm$	$100 \pm 9\,\mu N/m$	$40.0 \pm 0.5\,fm/\sqrt{Hz}$	
Silica in water AC-detector			
$16.2 \pm 0.4\,mV/nm$	$103 \pm 11\,\mu N/m$	$3.2 \pm 0.1\,fm/\sqrt{Hz}$	$1.40 \pm 0.02\,\mu m$
Silica in acetone AC-detector			
$6.3 \pm 0.2\,mV/nm$	$43 \pm 4\,\mu N/m$	$8.8 \pm 0.3\,fm/\sqrt{Hz}$	$1.97 \pm 0.03\,\mu m$

Table 4.1: Mean value and standard deviation of fitting parameters, determined through least squares fits of several independent data sets (The trapping strength k_{trap} is not an independent fitting parameter but is listed for completeness).

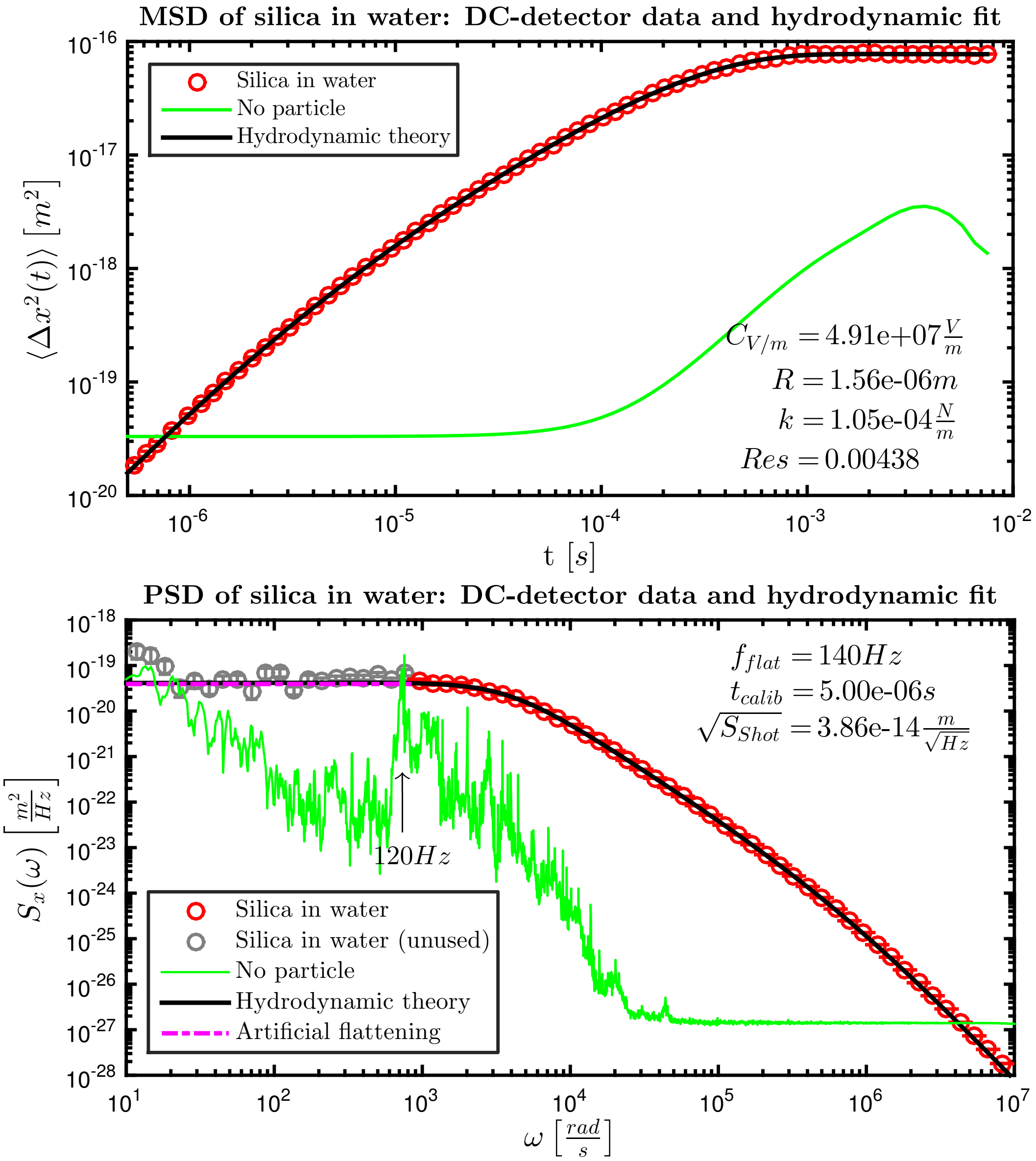

Figure 4.3: MSD and PSD for silica in water. The noise measurement of the PSD (green) has several resonance peaks due to vibration of the optics whose effect is bypassed by artificially flattening the PSD. The shot noise level has been fitted and subtracted from the signal.

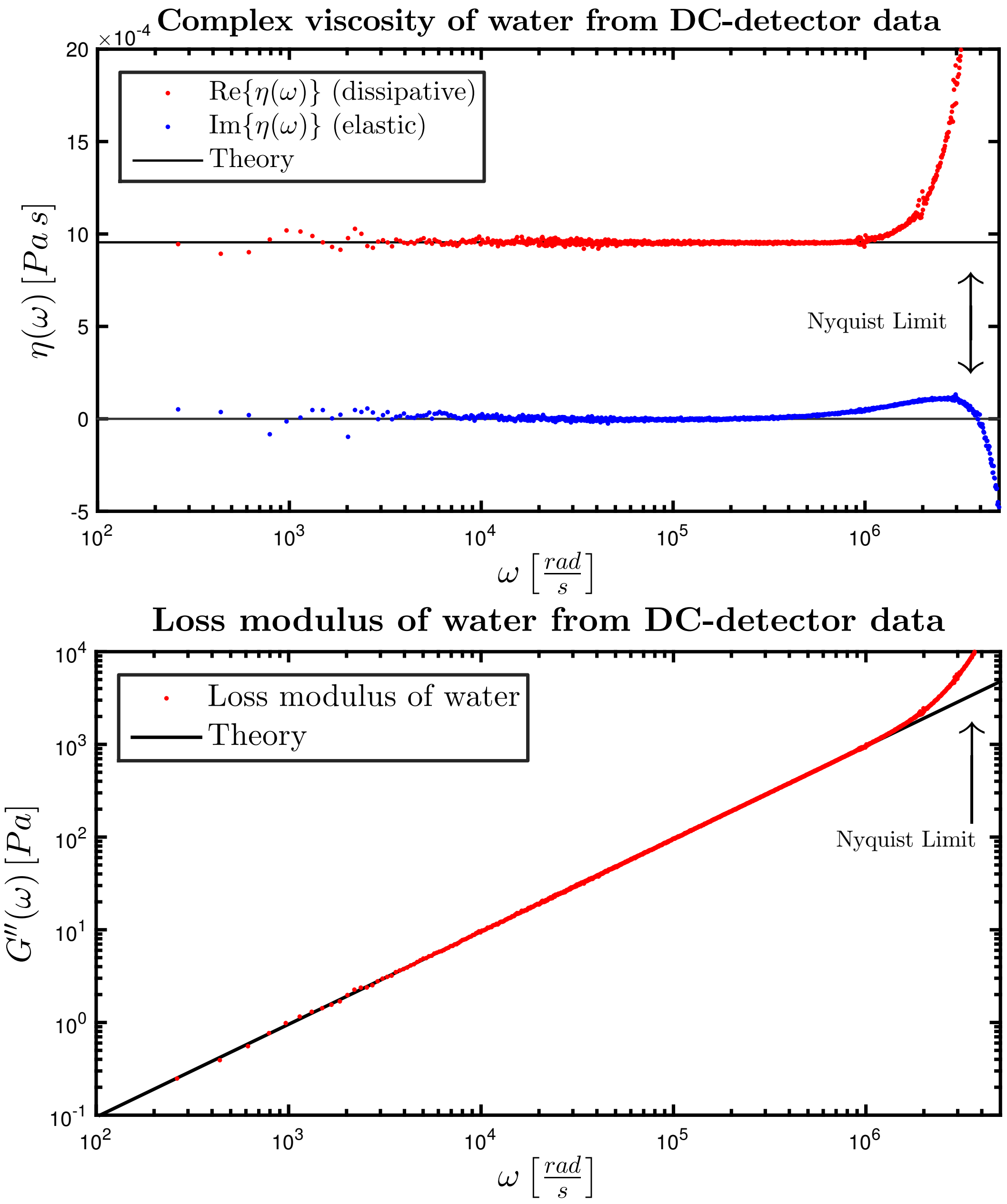

Figure 4.4: Complex viscosity and loss modulus of water from DC-detector data determined as mean value of 125 independent data sets. The smallest MSD input time for the calculation is $1\,\mu s$ and the determined viscosity is correct up to angular frequencies very close to the according Nyquist limit. For small ω, the impact of low frequency noise is noticable.

4.4.2 AC-detector results

Data analysis for the AC-detector data is similar, however, the artificial flattening has to be done at a higher frequency because of the in-built high pass filter, typically at $200\,Hz$. The design of the detector allows a detection power of around $150\,mW$ and accordingly the photon shot noise is smaller than for the DC-detector. It allows to determine the MSD at a smallest time of $t \approx 70\,ns$ compared to $1\,\mu s$ for the DC-detector and makes it possible to access higher frequencies. A typical fit is shown in Figure 4.5.

The downside is that the data doesn't fit as good to the theory as the DC-data. Flattening at too high frequencies leads to an overestimation of the trapping constant since it is

$$\int_{-\infty}^{\infty} S_x(\omega) d\omega = 2\pi \langle x^2 \rangle = 2\pi \frac{k_B T}{k} \tag{4.15}$$

and early flattening reduces the total area under the PSD. Flattening at too low frequencies introduces a systematical error because of the high pass filter. Flattening at $200\,Hz$ yields the same trapping strength at the same trapping power as the analysis of DC-detector data as shown in Table 4.1, which confirms the general validity of the fit. However the fitted radius deviates from the obtained radius of DC-detector data with the same bead trapped. Because of these fitting uncertainties, the calculated complex viscosity doesn't fit as perfectly as the one obtained from DC-data, but reaches one decade higher in angular frequency as shown in Figure 4.6. Plots of the acetone analysis can be found in Appendix B.

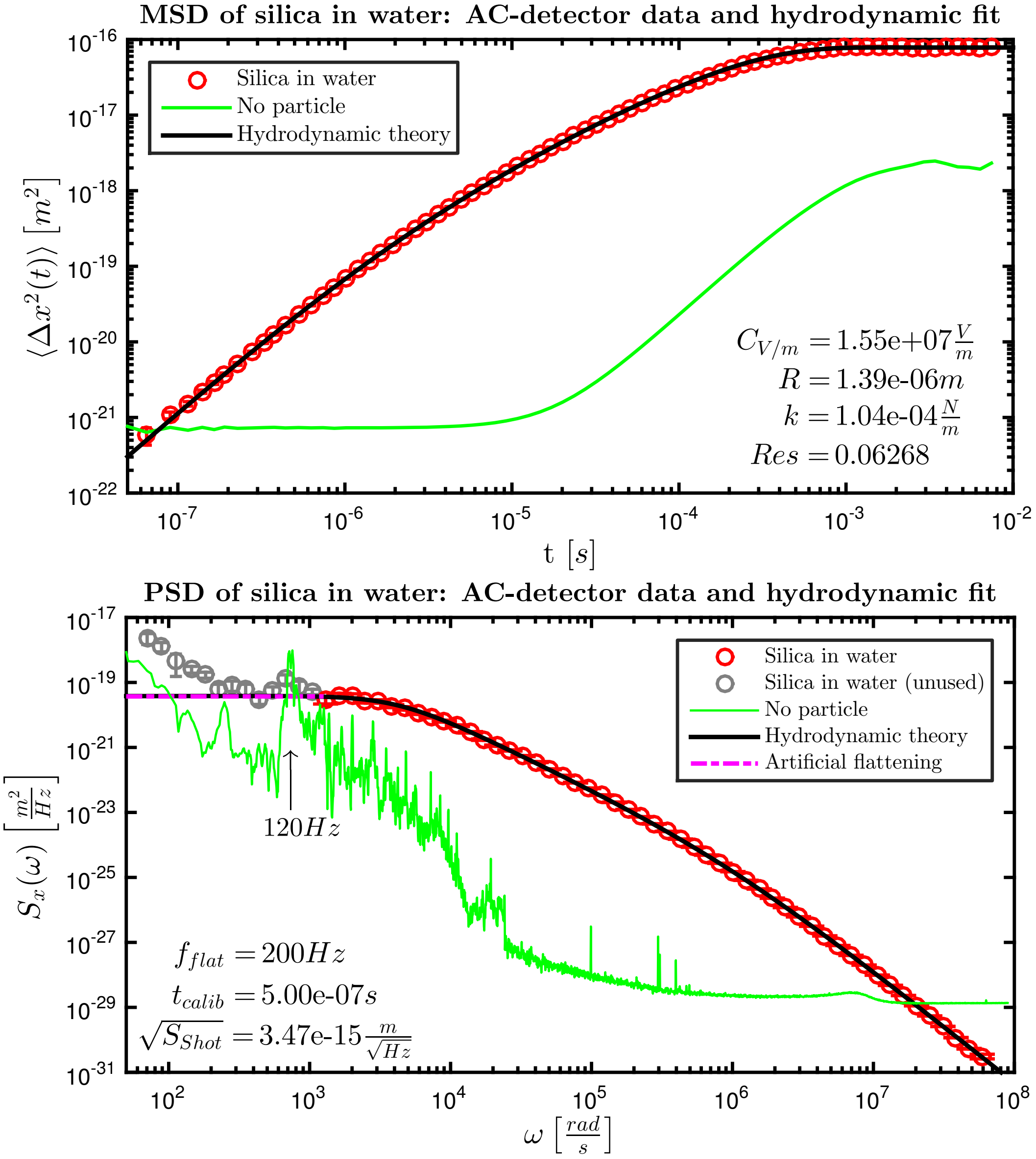

Figure 4.5: The AC-detector makes it possible to access approximately one decade higher in frequency than the DC-detector due to lower shot noise. However, the fit has a higher uncertainty because it has to be flattened at a higher frequency.

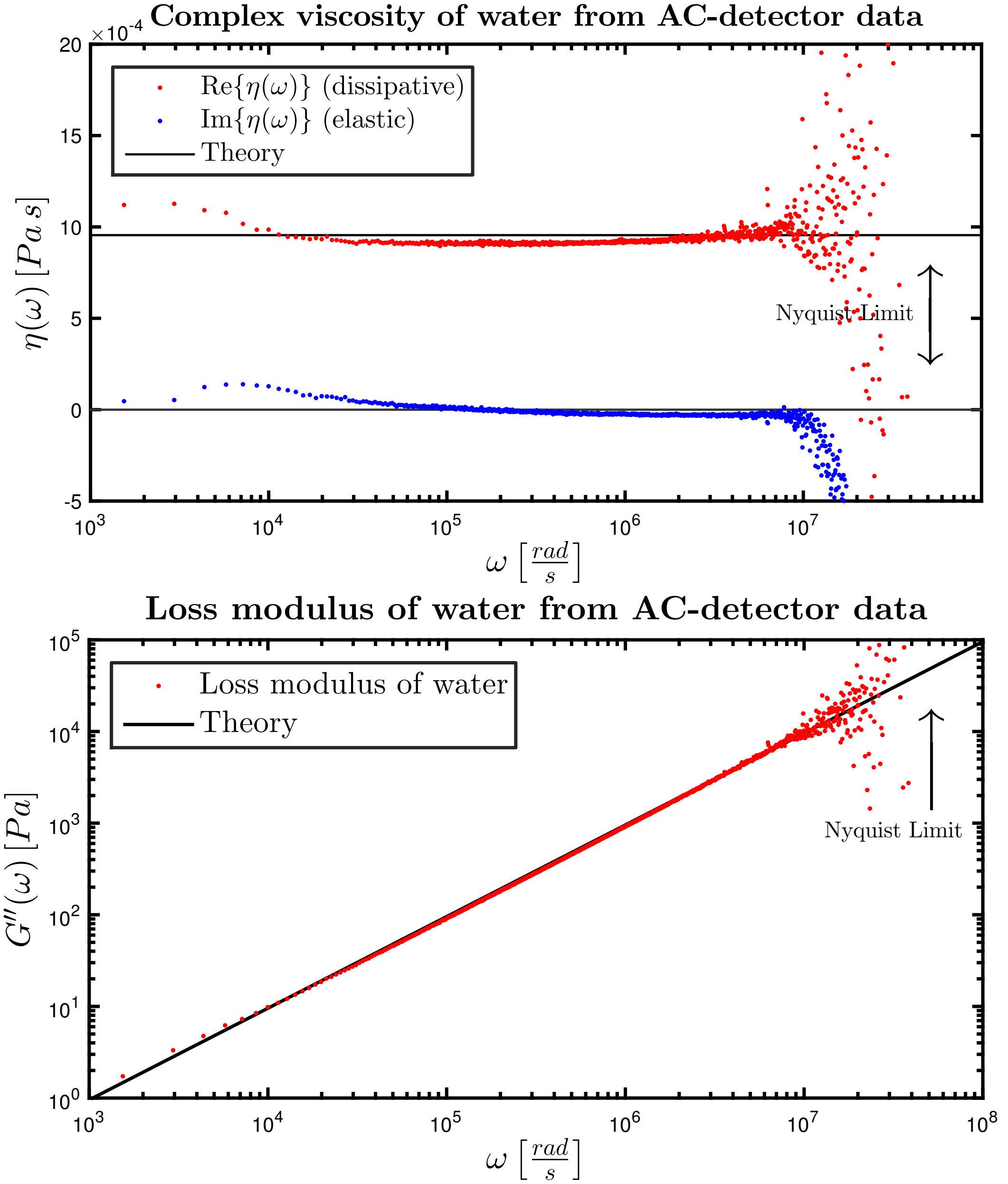

Figure 4.6: Complex viscosity and loss modulus of water from AC-detector data determined as mean value of 430 independent data sets. The smallest MSD input time for the calculation is $70\,ns$.

4.5 Conclusion and outlook

The previous chapters gave a detailed derivation of the theory of Brownian motion in complex fluids and the data analysis procedure to perform high frequency miorheology. The method was applied to data of Newtonian fluids where the rheological properties are known in order to verify it. The results show a very good agreement with the expected complex viscosity which is not only a verification of the microrheology data analysis procedure but also a strong validation of the hydrodynamic theory of Brownian motion in Newtonian fluids. To actually perform microrheology in complex fluids, however, introduces another difficulty.

In the previous data analysis, the volts to meter calibration, the trapping strength and the bead radius have been obtained by least squares fitting to the hydrodynamic theory, which is not possible for an unknown fluid. In order perform microrheology with Eq. (3.76), these parameters have to be obtained by another way. Moreover the steady state viscosity η_0 has to be known, which can be measured with a usual rherometer.

The easiest way to estimate unknown parameters is to perform a calibration experiment in a Newtonian fluid [3, 60, 61]. To do so, one first traps a bead in the Newtonian fluid and analyzes the data in order to obtain the volts to meter calibration constant $C_{V/m}$, the trapping strength k and the bead radius R as explained earlier. Then a sufficient amount of the desired complex fluid is pumped into the chamber with a low pumping speed, in order to keep the same bead trapped and to make the concentration of the calibration fluid negligible, which of course only works for appropriate fluids. Afterwards, the complex fluid data is taken without changing the alignment of the optics or the laser power. To obtain a good estimation, the index of refraction of the calibration fluid and the complex fluid should be as close as possible since the trapping strength and and the volts to meter calibration depend on the index of refraction mismatch of the trapped bead and the surrounding fluid.

Other approaches for calibration are to move the sample with a known amplitude and frequency by means of a piezoactuated translation stage [62], or to measure the particle relaxation to a discontinuously changing trap position [63].

Appendices

Appendix A

Additional theory

A.1 Proof of the Wiener-Khinchin theorem

The Wiener-Khinchin theorem states, that the correlation function of a random variable is given by the Fourier transform of its power spectral density. Starting with the definition of the correlation function in Eq. (3.2), one can write

$$\langle \xi(t)\xi(0)\rangle = \langle \xi(t)\xi^*(0)\rangle = \lim_{T\to\infty} \frac{1}{T}\int_{-T/2}^{T/2} \xi(t+\tau)\xi^*(\tau)d\tau$$

since the signal $\xi(t)$ is real valued, where the star denotes the complex conjugate. Now the following Fourier transformation convention for a time window T is applied,

$$\tilde{\xi}_k = \frac{1}{\sqrt{T}}\int_{-T/2}^{T/2} e^{i\omega_k t}\xi(t)dt \tag{A.1}$$

$$\xi(t) = \frac{1}{\sqrt{T}}\sum_{k=-\infty}^{+\infty} e^{-i\omega_k t}\tilde{\xi}_k \tag{A.2}$$

where the angular frequency

$$\omega_k = \frac{2\pi}{T}k \qquad k \in \mathbb{Z} \tag{A.3}$$

is discrete for a finite time window T. Consequently it is

$$\langle \xi(t)\xi(0)\rangle = \lim_{T\to\infty} \frac{1}{T^2}\int_{-T/2}^{T/2} \sum_{k,k'} \tilde{\xi}_k\tilde{\xi}^*_{k'} e^{-i\omega_k(t+\tau)}e^{i\omega_{k'}\tau}d\tau.$$

Taking the limit $T \to \infty$, ω becomes continuous

$$\omega_k \to \omega$$

$$\sum_{k,k'} \to \int \frac{d\omega d\omega'}{(2\pi/T)^2}.$$

$$\begin{aligned}\langle \xi(t)\xi(0)\rangle &= \frac{1}{(2\pi)^2}\int_{-\infty}^{\infty}\int_{-\infty}^{\infty}\int_{-\infty}^{\infty} e^{i\tau(\omega'-\omega)}e^{-i\omega t}\tilde{\xi}(\omega)\tilde{\xi}^*(\omega')d\omega d\omega' d\tau \\ &= \frac{1}{2\pi}\int_{-\infty}^{\infty}\int_{-\infty}^{\infty}\delta(\omega-\omega')e^{-i\omega t}\tilde{\xi}(\omega)\tilde{\xi}^*(\omega')d\omega d\omega' \\ &= \frac{1}{2\pi}\int_{-\infty}^{\infty} e^{-i\omega t}S_\xi(\omega)d\omega\end{aligned}$$

Inverse Fourier transform yields

$$S_\xi(\omega) = \int_{-\infty}^{\infty} e^{i\omega t}\langle \xi(t)\xi(0)\rangle dt. \tag{A.4}$$

A.2 Laplace transformation of the Basset force

The Laplace transform of a function $f(t)$ is given by

$$\mathcal{L}_t\left\{f(t)\right\} = \tilde{f}(s) = \int_0^{\infty} e^{-st}f(t)dt \tag{A.5}$$

with the inverse

$$\mathcal{L}_t^{-1}\left\{\tilde{f}(s)\right\} = f(t) = \frac{1}{2\pi i}\int_{c-i\infty}^{c+i\infty} e^{st}\tilde{f}(s)ds. \tag{A.6}$$

In order to write the Basset force in time domain by inverse Laplace transformation, the following identities are required [51]

$$\mathcal{L}_t\left\{\dot{f}(t)\right\} = s\tilde{f}(s) - f(0) \tag{A.7}$$

$$\mathcal{L}_t\left\{\frac{1}{\sqrt{t}}\right\} = \sqrt{\frac{\pi}{s}}. \tag{A.8}$$

One also needs to apply the convolution theorem for Laplace transformations which states, that a convolution in time domain is a simple product in the Laplace domain [51]

$$\mathcal{L}_t\left\{f(t)*g(t)\right\}=\mathcal{L}_t\left\{\int_0^t\left(f(t-\tau\right)g(\tau)d\tau\right\}=\mathcal{L}_t\left\{f(t)\right\}\mathcal{L}_t\left\{g(t)\right\}. \qquad \text{(A.9)}$$

Now, the inverse Laplace transformation of the Basset force is to be found with $s=-i\omega$

$$\mathcal{L}_t^{-1}\left\{\tilde{F}_{drag}(s)\right\}=\mathcal{L}_t^{-1}\left\{-6\pi\eta R\tilde{v}(s)-6\pi R^2\sqrt{s\rho_f\eta}\tilde{v}(s)-s\frac{2}{3}\pi R^3\rho_f\tilde{v}(s)\right\}.$$

The first and the last term are trivially found with Eq. (A.7) and the causality assumption $v(t\leq 0)=0$. For the square root term, it is

$$\begin{aligned}\mathcal{L}_t^{-1}\left\{\sqrt{s}\tilde{v}(s)\right\}&=\mathcal{L}_t^{-1}\left\{\frac{1}{\sqrt{s}}s\tilde{v}(s)\right\} &\text{(A.10)}\\ &=\mathcal{L}_t^{-1}\left\{\mathcal{L}_t\left\{\frac{1}{\sqrt{\pi t}}\right\}\mathcal{L}_t\left\{\dot{v}(t)\right\}\right\} &\text{(A.11)}\\ &=\frac{1}{\sqrt{\pi}}\mathcal{L}_t^{-1}\left\{\mathcal{L}_t\left\{\frac{1}{\sqrt{t}}*\dot{v}(t)\right\}\right\} &\text{(A.12)}\\ &=\frac{1}{\sqrt{\pi}}\int_0^t\frac{1}{\sqrt{t-t'}}\dot{v}(t')dt'. &\text{(A.13)}\end{aligned}$$

Consequently, it is

$$\mathcal{L}_t^{-1}\left\{\tilde{F}_{drag}(s)\right\}=-6\pi\eta Rv(t)-6R^2\sqrt{\pi\rho_f\eta}\int_0^t\frac{1}{\sqrt{t-t'}}\dot{v}(t')dt'-\frac{2}{3}\pi R^3\rho_f\dot{v}(t). \qquad \text{(A.14)}$$

A.3 Relation between the MSD and the VACF

The means square displacement of a Brownian particle is defined by

$$\langle \Delta x^2(t) \rangle = \langle [x(t) - x(0)]^2 \rangle. \tag{A.15}$$

The displacement can be written as

$$x(t) - x(0) = \int_0^t v(t')dt'. \tag{A.16}$$

and consequently it is

$$\langle \Delta x^2(t) \rangle = \int_0^t dt' \int_0^t \langle v(t')v(t'') \rangle dt'' = \int_0^t dt' \int_0^t C_v(t' - t'')dt''. \tag{A.17}$$

Substituting $\tau = t' - t''$ yields

$$\langle \Delta x^2(t) \rangle = \int_0^t dt' \int_{t'-t}^{t'} C_v(\tau)d\tau. \tag{A.18}$$

Figure A.3 illustrates, that the area of integration of Eq. (A.18) is a rhombus. Alternatively one can split the integral and integrate over two triangles which leads to

$$\langle \Delta x^2(t) \rangle = \underbrace{\int_{-t}^{0} C_v(\tau)d\tau \int_0^{t+\tau} dt'}_{\mathrm{I}} + \underbrace{\int_0^t C_v(\tau)d\tau \int_\tau^t dt'}_{\mathrm{II}}. \tag{A.19}$$

Substituting $\tau \to -\tau$ in the first term and using $C(\tau) = C(-\tau)$ yields [64]

$$\langle \Delta x^2(t) \rangle = 2 \int_0^t (t - \tau)\, C_v(\tau)d\tau. \tag{A.20}$$

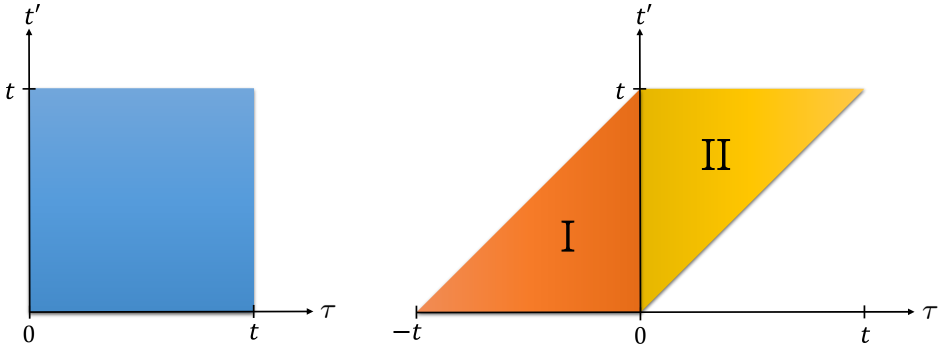

Figure A.1: The left side illustrates the integration area in Eq. (A.17). The right side shows the integration area after substituting to Eq. (A.18) and how it can be split into to integrations with triangular shape according to Eq. (A.19).

Eq. (A.20) can be further used to relate the MSD to the VACF in the Laplace domain. Applying the convolution theorem Eq. (A.9), one finds

$$\mathcal{L}_t\left\{\langle\Delta x^2(t)\rangle\right\} = \langle\Delta\tilde{x}^2(s)\rangle = 2\mathcal{L}_t\left\{t\right\}\mathcal{L}_t\left\{C_v(t)\right\} = \frac{2}{s^2}\tilde{C}_v(s). \tag{A.21}$$

With analytic continuation $s \to -i\omega$ one finds

$$\langle\Delta\tilde{x}^2(\omega)\rangle = -\frac{2}{\omega^2}\tilde{C}_v(\omega). \tag{A.22}$$

A.4 Solutions of the generalized Langevin Equation

This appendix lists analytic solutions of Eq. (3.43). The position PSD reads [34, 65]

$$S_x(\omega) = \frac{2k_BT}{\gamma_s\omega^2}\frac{1+\sqrt{|\omega|\tau_f/2}}{\left(1/(|\omega|\tau_k) - \sqrt{|\omega|\tau_f/2} - |\omega|\tau_p - |\omega|\tau_f/9\right)^2 + \left(1+\sqrt{|\omega|\tau_f/2}\right)^2}. \tag{A.23}$$

The mean square displacement is [47, 65]

$$\begin{aligned}\langle[\Delta x^2(t)]\rangle = \frac{2k_BT}{k} + \frac{2k_BT}{m^*}\Bigg[&\frac{e^{z_1^2t}\,\mathrm{erfc}(z_1\sqrt{t})}{z_1(z_1-z_2)(z_1-z_3)(z_1-z_4)}\\ &+\frac{e^{z_2^2t}\,\mathrm{erfc}(z_2\sqrt{t})}{z_2(z_2-z_1)(z_2-z_3)(z_2-z_4)}\\ &+\frac{e^{z_3^2t}\,\mathrm{erfc}(z_3\sqrt{t})}{z_3(z_3-z_1)(z_3-z_2)(z_3-z_4)}\\ &+\frac{e^{z_4^2t}\,\mathrm{erfc}(z_4\sqrt{t})}{z_4(z_4-z_1)(z_4-z_2)(z_4-z_3)}\Bigg].\end{aligned} \tag{A.24}$$

Finally the velocity autocorrelation function is found to be [47, 65]

$$\begin{aligned}C_v(t) = \frac{k_BT}{m^*}\Bigg[&\frac{z_1^3e^{z_1^2t}\,\mathrm{erfc}(z_1\sqrt{t})}{(z_1-z_2)(z_1-z_3)(z_1-z_4)} + \frac{z_2^3e^{z_2^2t}\,\mathrm{erfc}(z_2\sqrt{t})}{(z_2-z_1)(z_2-z_3)(z_2-z_4)}\\ &+\frac{z_3^3e^{z_3^2t}\,\mathrm{erfc}(z_3\sqrt{t})}{(z_3-z_1)(z_3-z_2)(z_3-z_4)} + \frac{z_4^3e^{z_4^2t}\,\mathrm{erfc}(z_4\sqrt{t})}{(z_4-z_1)(z_4-z_2)(z_4-z_3)}\Bigg].\end{aligned} \tag{A.25}$$

The coefficients z_1, z_2, z_3 and z_4 are the four roots of the equation [65]

$$\left(\tau_p + \frac{1}{9}\tau_f\right)z^4 - \sqrt{\tau_f}z^3 + z^2 + \frac{1}{\tau_k} = 0. \tag{A.26}$$

Appendix B

Microrheological results for acetone

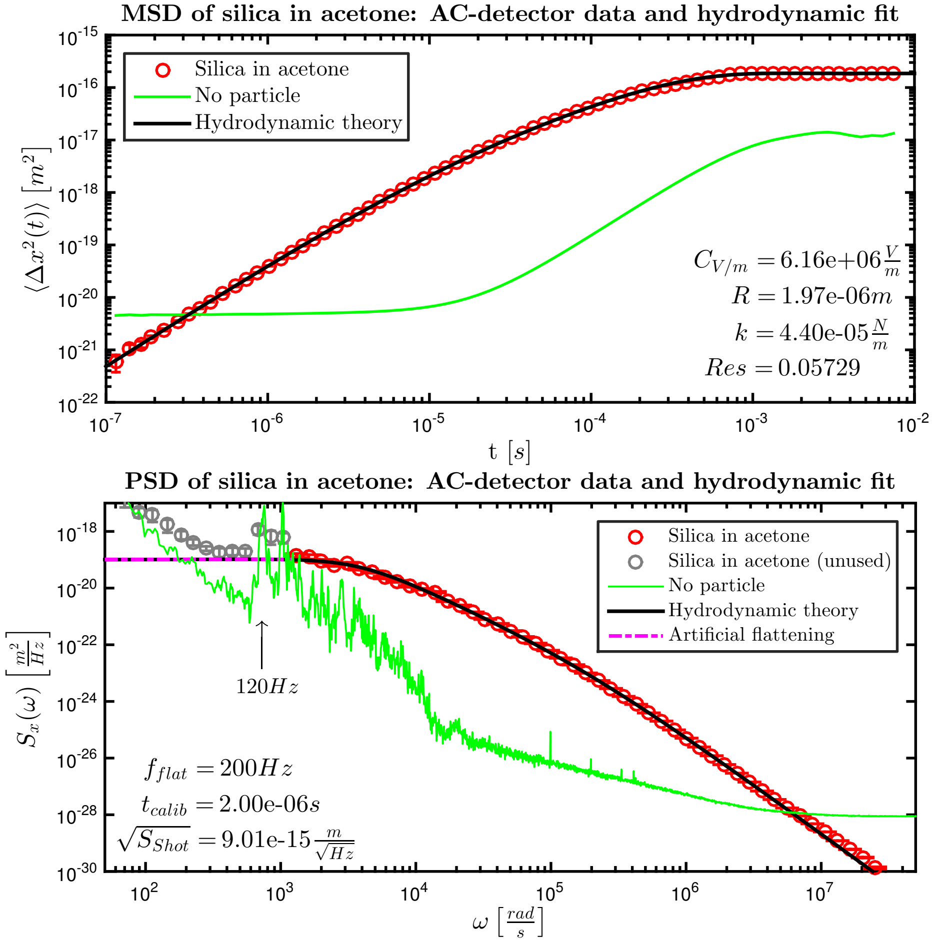

Figure B.1: MSD and PSD for silica in acetone. The shot noise level is higher compared to the measurements in water.

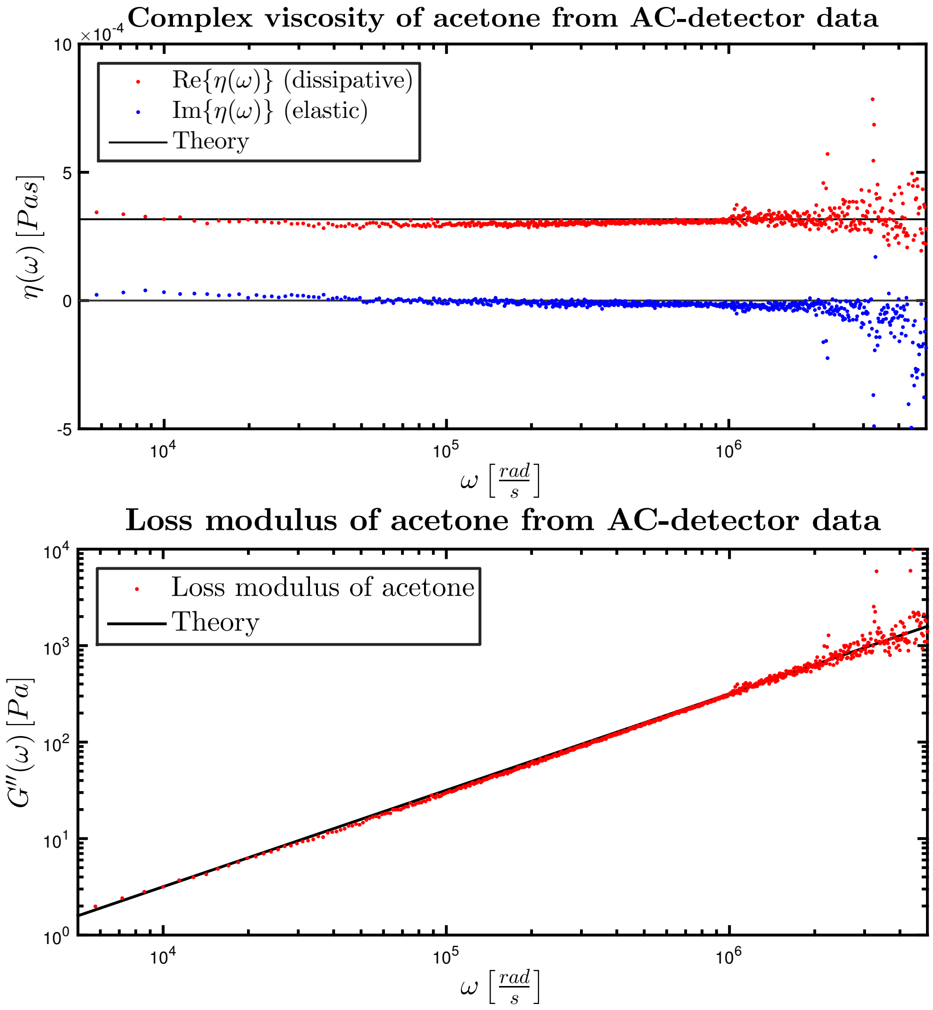

Figure B.2: Complex viscosity and loss modulus of acetone from AC-detector data determined as mean value of 41 independent data sets. The smallest MSD input time for the calculation is $200\,ns$. The peaks at $\omega > 10^6\,rad/s$ are due to laser intensity noise and misalignment of the D-shaped mirror.

Appendix C

Numerical Laplace transformation

In order to perform high frequency microrheology, a very decent Laplace transform algorithm is required to obtain accuracy. Evans et al. introduced a strong algorithm in 2009, which interpolates a data set with N points as a piecewise linear function and then analytically calculates the Laplace transform [55, 57]

$$\tilde{f}(\omega) = \mathcal{L}_t \left\{ f(t) \right\} \Big|_{s=-i\omega} = \frac{i}{\omega} f(0)$$
$$+ \frac{1}{\omega^2} \left[\frac{f(t_1) - f(0)}{t^1} \left(e^{i\omega t_1} - 1 \right) - \dot{f}_\infty e^{i\omega t_N} + \sum_{k=2}^{N} \frac{f(t_k) - f(t_{k-1})}{t_k - t_{k-1}} \left(e^{i\omega t_k} - e^{i\omega t_{k-1}} \right) \right]. \tag{C.1}$$

It includes an extrapolation $f(0)$ to $t = 0$ and an extrapolation to infinity with $\dot{f}_\infty$ being the gradient of f extrapolated to infinity.

This algorithm can be further improved by applying a quadratic interpolation between each three points instead of a linear interpolation, which is relevant for high frequencies. A parabola

$$P(t) = at^2 + bt + c \tag{C.2}$$

is uniquely determined by a set of three points $\{t_n/f(t_n)\}, \{t_{n+1}/f(t_{n+1})\}$ and $\{t_{n+2}/f(t_{n+2})\}$ with $t_n \neq t_{n+1} \neq t_{n+2}$. The coefficients a_n, b_n and c_n of the parabola between t_n and t_{n+2} can be determined by solving the linear system

$$\begin{pmatrix} t_n^2 & t_n & 1 \\ t_{n+1}^2 & t_{n+1} & 1 \\ t_{n+2}^2 & t_{n+2} & 1 \end{pmatrix} \begin{pmatrix} a_n \\ b_n \\ c_n \end{pmatrix} = \begin{pmatrix} f(t_n) \\ f(t_{n+1}) \\ f(t_{n+2}) \end{pmatrix} . \tag{C.3}$$

Now, the total Laplace integral is decomposed into a sum of Laplace integrals over parabolas:

$$\begin{aligned} \int_0^\infty e^{i\omega t} f(t) &\approx \sum_{\text{even } n} \int_{t_n}^{t_{n+2}} e^{i\omega t} \left(a_n t^2 + b_n t + c_n\right) dt \\ &= \sum_{\text{even } n} - \left[\frac{i}{\omega} e^{i\omega t} \left(a_n t^2 + b_n t + c_n\right)\right]\Bigg|_{t_n}^{t_{n+2}} \\ &\quad + \left[\frac{1}{\omega^2} e^{i\omega t} \left(2a_n t + b_n\right)\right]\Bigg|_{t_n}^{t_{n+2}} + \left[\frac{i}{\omega^3} e^{i\omega t} 2a_n\right]\Bigg|_{t_n}^{t_{n+2}} \end{aligned} \tag{C.4}$$

Since the parabola segments are continuous at the transitions, it is

$$e^{i\omega t} \left(a_n t^2 + b_n t + c_n\right)\Big|_{t=t_{n+2}} = e^{i\omega t} \left(a_{n+2} t^2 + b_{n+2} t + c_{n+2}\right)\Big|_{t=t_{n+2}} . \tag{C.5}$$

Consequently, the first term in Eq. (C.4) mostly vanishes by performing the sum. The only terms left is for $n = 0$ and $n = N - 2$ because there exists no according summand to cancel with. The last term is negligible, assuming that $f \to 0$ as $t \to \infty$. In other cases one can design an extrapolation to infinity similarly as done in Eq. (C.1). The first $n = 0$ term needs to be kept and is used to do an extrapolation to $t = 0$.

Consequently one finds for the Laplace transformation of a data set $\{t_n/f(t_n)\}$ of even size, starting at $n = 1$ with extrapolation to zero $\{t_0 = 0/f(t_0 = 0)\}$, where the time array must not be equally spaced:

$$\tilde{f}(\omega) = \mathcal{L}_t\left\{f(t)\right\}\Big|_{s=-i\omega} = \frac{i}{\omega}c_0 + \frac{1}{\omega^2}\left[e^{i\omega t_2}\left(2a_0 t_2 + b_0\right) - b_0\right] + \frac{i}{\omega_3}2a_0\left(e^{i\omega t_2} - 1\right)$$
$$+ \sum_{\text{even } n=2}^{N-2} \frac{1}{\omega^2}\left[e^{i\omega t_{n+2}}\left(2a_n t_{n+2} + b_n\right) - e^{i\omega t_n}\left(2a_n t_n + b_n\right)\right] + \frac{i}{\omega^3}2a_n\left(e^{i\omega t_{n+2}} - e^{i\omega t_n}\right), \tag{C.6}$$

the coefficients have to be determined for each interval respectively. Solving Eq. (C.3) yields with the abbreviation $f(t_n) \equiv f_n$

$$a_n = \frac{(-f_n + f_{n+1})t_{n+2} + (f_n - f_{n+2})t_{n+1} + (-f_{n+1} + f_{n+2})t_n}{(t_n - t_{n+1})(t_n - t_{n+2})(t_{n+1} - t_{n+2})} \tag{C.7}$$

$$b_n = \frac{(f_n - f_{n+1})t_{n+2}^2 + (-f_n + f_{n+2})t_{n+1}^2 + (f_{n+1} - f_{n+2})t_n^2}{(t_n - t_{n+1})(t_n - t_{n+2})(t_{n+1} - t_{n+2})} \tag{C.8}$$

$$c_n = \frac{(-f_n t_{n+1} + f_{n+1} t_n)t_{n+2}^2 + (f_n t_{n+2} - f_{n+2} t_n)t_{n+1}^2 + (-f_{n+1} t_{n+2} + f_{n+2} t_{n+1})t_n^2}{(t_n - t_{n+1})(t_n - t_{n+2})(t_{n+1} - t_{n+2})}. \tag{C.9}$$

Bibliography

[1] M. Tassieri, R.M.L. Evans, R.L. Warren, N.J. Bailey, and J.M. Cooper. Microrheology with optical tweezers: data analysis. *New Journal of Physics*, 14:1–19, 2012.

[2] Christopher J. Pipe, Trushant S. Majmudar, and Gareth H. McKinley. High shear rate viscometry. *Rheologica Acta*, 47:621–642, 2008.

[3] Giuseppe Pesce, Giulia Rusciano, and Antonio Sasso. Blinking Optical Tweezers for microrheology measurements of weak elasticity complex fluids. *Optics express*, 18(3):2116–2126, 2010.

[4] Pietro Cicuta and Athene M. Donald. Microrheology: a review of the method and applications. *Soft Matter*, 3:1449–1455, 2007.

[5] Ben Fabry, Geoffrey N. Maksym, James P. Butler, Michael Glogauer, Daniel Navajas, and Jeffrey J. Fredberg. Scaling the microrheology of living cells. *Phys. Rev. Lett.*, 87:1–4, 2001.

[6] Philip Kollmannsberger and Ben Fabry. Linear and nonlinear rheology of living cells. *Annual Review of Materials Research*, 41:75–97, 2011.

[7] C. Oelschlaeger, M. Cota Pinto Coelho, and N. Willenbacher. Chain flexibility and dynamics of polysaccharide hyaluronan in entangled solu-

tions: A high frequency rheology and diffusing wave spectroscopy study. *Biomacromolecules*, 14:3689–3696, 2013.

[8] D. C. Vadillo, T. R. Tuladhar, A. C. Mulji, and M. R. Mackley. The rheological characterization of linear viscoelasticity for ink jet fluids using piezo axial vibrator and torsion resonator rheometers. *Journal of Rheology*, 54:781–795, 2012.

[9] T.A. Waigh. Microrheology of complex fluids. *Rep. Prog. Phys.*, 68:685–742, 2005.

[10] T.G. Mason and D.A. Weitz. Optical measurements of frequency-dependent linear viscoelastic moduli of complex fluids. *Phys. Rev. Lett.*, 74(7):1250–1253, 1995.

[11] B. U. Felderhof. Estimating the viscoelastic moduli of a complex fluid from observation of Brownian motion. *J. Chem. Phys.*, 131:1–7, 2009.

[12] B. U. Felderhof. Estimating the viscoelastic moduli of complex fluids from observation of Brownian motion of a particle confined to a harmonic trap. *Journal of Chemical Physics*, 134, 2011.

[13] Tsutomu Indei, Jay D. Schieber, and A. Córdoba. Treating inertia in passive microbead rheology. *Rhys. Rev. E*, 85:1–18, 2012.

[14] J.C. Maxwell. *A treatise on electricity and magnetism.* Oxford, 1873.

[15] P. N. Lebedev. Untersuchungen über die Druckkräfte des Lichtes. *Ann. Phys.*, 311(11):433–458, 1901.

[16] E. F. Nichols and G. F. Hull. A preliminary communication on the pressure of heat and light radiation. *Physical Review (Series I)*, 13(5):307–320, 1901.

[17] A. Ashkin. History of optical trapping and manipulation of small-neutral particle, atoms, and molecules. *IEEE Journal on Selected Topics in Quantum Electronics*, 6(6):841–856, 2000.

[18] A. Ashkin. Acceleration and trapping of particles by radiation pressure. *Phys. Rev. Lett.*, 24(4):156–159, 1970.

[19] A. Ashkin, J. M. Dziedzic, J. E. Bjorkholm, and S. Chu. Observation of a single-beam gradient force optical trap for dielectric particles. *Optics letters*, 11(5):288–290, 1986.

[20] A. Ashkin. Optical trapping and manipulation of viruses and bacteria. *Science*, 235:1517–1520, 1987.

[21] Timo A. Nieminen, Vincent L. Y. Loke, Alexander B. Stilgoe, Gregor Knöner, Agata M. Braczyk, Norman R. Heckenberg, and Halina Rubinsztein-Dunlop. Optical tweezers computational toolbox. *Journal of Optics A: Pure and Applied Optics*, 9(8):196–203, 2007.

[22] A Ashkin. Forces of a single-beam gradient laser trap on a dielectric sphere in the ray optics regime. *Biophys. J.*, 61:569–582, 1992.

[23] Yasuhiro Harada and Toshimitsu Asakura. Radiation forces on a dielectric sphere in the Rayleigh scattering regime. *Optics Communications*, 124: 529–541, 1996.

[24] F. Gittes and C. F. Schmidt. Interference model for back-focal-plane displacement detection in optical tweezers. *Optics letters*, 23(1):7–9, 1998.

[25] M. W. Allersma, F. Gittes, M. J. DeCastro, R. J. Stewart, and C. F. Schmidt. Two-dimensional tracking of ncd motility by back focal plane interferometry. *Biophysical journal*, 74:1074–1085, 1998.

[26] K. Visscher, S.P. Gross, and S.M. Block. Construction of multiple-beam optical traps with nnanometer-resolution position sensing. *IEEE Journal of Selected Topics in Quantum Electronics*, 2(4):1066–1076, 1996.

[27] A. Pralle, M. Prummer, E. L. Florin, E. H. K. Stelzer, and J. K. H. Hörber. Three-dimensional position tracking for optical tweezers by forward scattered light. *Microscopy Research and Technique*, 44:378–386, 1999.

[28] Isaac Chavez, Rongxin Huang, Kevin Henderson, Ernst Ludwig Florin, and Mark G. Raizen. Development of a fast position-sensitive laser beam detector. *Review of Scientific Instruments*, 79(10):3–5, 2008.

[29] Simon Kheifets. *High-sensitivity tracking of optically trapped particles in gasses and liquids : observation of Brownian motion in velocity space.* PhD thesis, 2014.

[30] Jianyong Mo, Akarsh Simha, Simon Kheifets, and Mark G Raizen. Testing the Maxwell-Boltzmann distribution using Brownian particles. *Optics Express*, 23(2):1888–1893, 2015.

[31] Frederick Gittes and Christoph F. Schmidt. Signals and Noise in Micromechanical Measurements. *Methods in cell biology*, 55:129–156, 1998.

[32] Robert Brown. A brief account of microscopical observations on the particles contained in the pollen of plants. *Philosophical Magazine Series 2*, 4(21):161–173, 1828.

[33] V. Balakrishnan. *Elements of Nonequilibrium Statistical Mechanics*. Ane Books India, 2008.

[34] Kirstine Berg-Sørensen and Henrik Flyvbjerg. Power spectrum analysis for optical tweezers. *Review of Scientific Instruments*, 75(3):594–612, 2004.

[35] Eric W. Weisstein. 'Wiener-Khinchin Theorem' From MathWorld - A Wolfram web resource. URL `http://mathworld.wolfram.com/Wiener-KhinchinTheorem.html`.

[36] A. Khintchine. Korrelationstheorie der stationären stochastischen Prozesse. *Mathematische Annalen*, 109:604–615, 1934.

[37] R. Kubo. The fluctuation-dissipation theorem. *Reports on progress in physics*, 29(1):255–283, 1966.

[38] Albert Einstein. Über die von der molekularkinetischen Theorie der Wärme geforderte Bewegung von in ruhenden Flüssigkeiten suspendierten Teilchen. *Ann. Phys. (Leipzig)*, 17:549–560, 1905.

[39] Paul Langevin. Sur la théorie du mouvement Brownien. *C.R. Acad. Sci.*, 146:530–533, 1908.

[40] G.E. Uhlenbeck and L.S. Ornstein. On the theory of the Brownian motion. *Phys. Rev.*, 36:823–841, 1930.

[41] M.C. Wang and G.E. Uhlenbeck. On the Theory of the Brownian motion II. *Rev. of Modern Physics*, 17:323–342, 1945.

[42] G. G. Stokes. On the effect of the internal friction of fluids on the motion of pendulums. *Transactions of the Cambridge Philosophical Society*, 9, 1851.

[43] Jay D. Schieber, Andrés Córdoba, and Tsutomu Indei. The analytic solution of Stokes for time-dependent creeping flow around a sphere: Application to linear viscoelasticity as an ingredient for the generalized Stokes-Einstein relation and microrheology analysis. *Journal of Non-Newtonian Fluid Mechanics*, 200:3–8, 2013.

[44] L.D. Landau and E.M. Lifshitz. *Fluid Mechanics.* Pergamon Books Ltd., 1987.

[45] A. B. Basset. On the motion of a sphere in a viscous liquid. *Phil. Trans. R. Soc. Lond. A*, 179:43–63, 1888.

[46] J. Boussinesq. Sur la résistance qu'oppose un fluide indéfini en repos, sans pesanteur, au mouvement varié d'une sphère solide qu'il mouille sur toute sa surface, quand les vitesses restent bien continues et assez faibles pour que leurs carrés et produits soient néglige. 100:935–937, 1885.

[47] H. J. H. Clercx and P. P. J. M. Schram. Brownian particles in shear-flow and harmonic potentials: A study of long-time tails. *Physical Review A*, 46(4):1942–1950, 1992.

[48] Robert Zwanzig and Mordechai Bixon. Compressibility effects in the hydrodynamic theory of Brownian motion. *Journal of Fluid Mechanics*, 69(1):21–25, 1975.

[49] P. Oswald. *Rheophysics, the deformation and flow of matter*. Cambridge University Press, 2009.

[50] Matthias Grimm, Sylvia Jeney, and Thomas Franosch. Brownian motion in a Maxwell fluid. *Soft Matter*, 7:2076–2084, 2011.

[51] Milton Abramowitz and A. Irene Stegun. *Handbook of Mathematical Functions with Formulas, Graphs, and Mathematical Tables*. 1972.

[52] T. G. Mason, Hu Gang, and D. A. Weitz. Diffusing-wave-spectroscopy measurements of viscoelasticity of complex fluids. *Journal of the Optical Society of America A*, 14(1):139–149, 1997.

[53] Thomas G. Mason. Estimating the viscoelastic moduli of complex fluids using the generalized Stokes-Einstein equation. *Rheologica Acta*, 39:371–378, 2000.

[54] Todd M. Squires and Thomas G. Mason. Fluid fechanics of microrheology. *Annual Review of Fluid Mechanics*, 42(1):413–438, 2010.

[55] Manlio Tassieri, Graham M. Gibson, R. M. L. Evans, Alison M. Yao, Rebecca Warren, Miles J. Padgett, and Jonathan M. Cooper. Measuring storage and loss moduli using optical tweezers: Broadband microrheology. *Physical Review E - Statistical, Nonlinear, and Soft Matter Physics*, 81: 1–5, 2009.

[56] Claude E. Shannon. Communication in the presence of noise. *Proceedings of the I.R.E*, 37:10–21, 1949.

[57] R. M. L. Evans, Manlio Tassieri, Dietmar Auhl, and Thomas A. Waigh. Direct conversion of rheological compliance measurements into storage and loss moduli. *Physical Review E - Statistical, Nonlinear, and Soft Matter Physics*, 80(1):012501, 2009.

[58] E.-L. Florin, A. Pralle, E.H.K. Stelzer, and J.K.H. Hörber. Photonic force microscope calibration by thermal noise analysis. *Applied Physics A: Materials Science & Processing*, 66:75–78, 1998.

[59] Tongcang Li and Mark G. Raizen. Brownian motion at short time scales. *Annalen der Physik*, 525(4):281–295, 2013.

[60] P. Domínguez-García, Frédéric Cardinaux, Elena Bertseva, László Forró, Frank Scheffold, and Sylvia Jeney. Accounting for inertia effects to access the high-frequency microrheology of viscoelastic fluids. *Phys. Rev. E*, 90 (6):1–5, 2014.

[61] Laurence Wilson, Rut Besseling, Jochen Arlt, and Wilson C.K. Poon. Linear and nonlinear microrheology of dense colloidal suspensions. *Proc. of SPIE - The international society for optical engineering*, 6326:1–10, 2006.

[62] B. Schnurr, F. Gittes, F. C. MacKintosh, and C. F. Schmidt. Determining microscopic viscoelasticity in flexible and semiflexible polymer networks from thermal fluctuations. *Macromolecules*, 30(25):7781–7792, 1997.

[63] Matthew M. Shindel, James W. Swan, and Eric M. Furst. Calibration of an optical tweezer microrheometer by sequential impulse response. *Rheologica Acta*, 52:455–465, 2013.

[64] J. P. Boon and S. Yip. *Molecular Hydrodynamics.* Dover Publications, 1991.

[65] Branimir Lukić, Sylvia Jeney, Željko Sviben, Andrzej J. Kulik, Ernst Ludwig Florin, and László Forró. Motion of a colloidal particle in an optical trap. *Physical Review E - Statistical, Nonlinear, and Soft Matter Physics*, 76:1–9, 2007.

Vita

David Riegler was born in Engelskirchen, Germany. He graduated with the German Abitur at the Rhoengymnasium in Bad Neustadt, Bavaria in 2010 with a prize of the DPG (German Physical Society) for outstanding performance in the subject physics. After working at a hospital for half a year as mandatory civil service, he started the Bachelor of Physics at the Julius-Maximilians-Universitaet in Wuerzburg in the spring of 2011. He graduated with the B.S. in Physics in summer 2014 and entered the graduate school of the University of Texas at Austin in fall 2014. From 9/2014 until 5/2015 he received a scholarship from the German Academic Exchange Service (DAAD).

Email address: david.riegler@utexas.edu

This thesis was typeset with LaTeX[†] by David Riegler.

[†] LaTeX is a document preparation system developed by Leslie Lamport as a special version of Donald Knuth's TeX Program.